APPLICATIONS OF FINITE ELEMENT METHOD IN STUDYING MECHANICAL BEHAVIOR OF CONCRETE MATERIALS ON DIFFERENT SCALES

BY

CHUANYUE SHEN

THESIS

Submitted in partial fulfillment of the requirements
for the degree of Master of Science in Civil Engineering
in the Graduate College of the
University of Illinois at Urbana-Champaign, 2018

Urbana, Illinois

Advisor:

Professor David A. Lange

ABSTRACT

Computer simulation is a powerful tool for understanding material behavior at a wide range of scales. This research uses finite element modeling for two investigations at two very different scales.

The first study considers the microstructure of foam concrete material. The objective is providing insights for understanding the foam concrete crushing behavior, where the real foam concrete microstructure is studied. With a micro-CT scan providing the foam geometry information, tetrahedral meshes are generated for rendering the microstructure, which is further used for simulating a uniaxial compression test in Abaqus/CAE. The simulation result is qualitatively reasonable, suggesting a potential of using this approach for further exploring the foam crushing behavior.

The second study focuses on investigating the thermal induced movement of the full-scale airport slabs at O'Hare International Airport. The simulation is implemented to evaluate four model configurations for estimating the opening at concrete expansion joints. After further considering the actual boundary condition, the modeling effort demonstrates acceptable accuracy of the simulation result. The good agreement between the FEM simulation and the field measurement confirms a realistic prediction overall. By studying the stress concentration in the concrete slabs in subsequent, it is found that expansion joint width plays the most critical role in alleviating the stress buildup issue as concerned by the field engineers.

ACKNOWLEDGEMENTS

This report is a thesis presented by Chuanyue Shen in partial fulfillment of the requirements for the Master of Science degree. First and foremost, I would like to express my sincere gratitude to my advisor Professor David A. Lange for offering me the opportunity to be part of these research projects. Without his continuous support and guidance, the research work and this thesis would hardly have been completed. His patience, understanding, encouragement and insights inspire me moving forward.

I appreciate the financial support made possible by the University Transportation Center (UTC) Research on Concrete Applications for Sustainable Transportation (RE-CAST) based at Missouri University of Science and Technology. I also gratefully acknowledge support from the O'hare Modernization Program and Chicago Department of Aviation for funding related to the slab displacement project.

I would like to thank all those who helped me in accomplishing the research work. Special thanks to Yu Song who provided me with guidance on my Master study. Thanks to Jamie Clark for providing the foam concrete micro-CT scan for analysis. Thanks to Kate Hawkins and Karthik Pattaje S. for kind encouragement and advice.

I must express my very profound gratitude and love to my parents for providing me with unfailing support and continuous encouragement.

TABLE OF CONTENTS

CHAPTER 1. INTRODUCTION

Concrete is one of the most common construction materials. It possesses not only a high structural capacity but also durable and sustainable advantages. These features make it suitable to be used for building, bridge, dam, and pavement constructions. To better understand the concrete mechanical performance, it is necessary to investigate its loading behavior. Physical experiments, such as compression and tensile tests, are broadly adopted to characterize the concrete mechanics. However, they can be restricted by the object scale, experimental condition, environmental condition, and economic factors. In comparison, computer simulation, as an imitation of the real-world scenario, is more flexible and compensative for providing comprehensive understanding of the material behavior.

Finite element method (FEM) can be used for concrete material research under different scales and different influences. This study focuses on using this method for characterizing the mechanical behavior of foam concrete on a micro scale and conventional concrete slab movement on a macro scale. The first part of the study aims at investigating the foam concrete microstructure. Foam concrete experiences large deformation and absorbs a substantial amount of energy in a crushing event. This unique crushing behavior is attributed to its cellularized structure. As such, it is essential to study the responses of the microstructure under loading. An approach for restoring the foam concrete microstructure for FEM analysis is presented in Chapter 2.

The second inspection is conducted on full-scale airport slabs at O'Hare International Airport. These slabs exhibit evident movements, which is suspected to be the cause of persistent liquid leakage in the underground tunnel. The slab movement is induced by the temperature change.

Hence, full-scale airport slabs are modeled, and their thermal responses are studied. Chapter 3 provides the detailed model configurations and related analysis.

CHAPTER 2. FINITE ELEMENT MODELING OF FOAM CONCRETE CRUSHING BEHAVIOR

2.1 Introduction

Foam concrete is a light-weight construction material that usually made of water, cement, foaming agent and chemical additives (such as accelerator and water reducer). As shown in Figure 2.1, foam concrete is an interconnection of solid struts and plates, which form walls and faces of cells. Owing to the high void content, foam concrete is highly cellularized and light-weight with a density ranging from 300 to 1600 kg/m^3 and a compressive strength of 1 to 10 N/mm^2 [1]. These values are significantly low as compared to conventional concrete materials. Thus, foam concrete is also known as a type of cellular concrete [2], lightweight concrete [3], and low-density controlled low-strength material (LD-CLSM) [4].

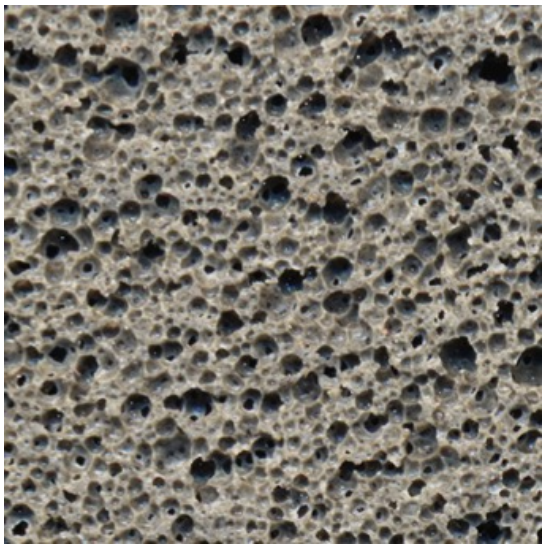

Figure 2.1: 0.6 g/cc foam concrete.

In some cases, recycled fine materials could be introduced to the fresh mixture to enhance the foam concrete strength. Recycling aggregate materials from building demolition have been reused in

constructions because of the increasing demand for aggregates and the need for deposing construction waste both economic and environmental friendly [5]. Many states are seeking the applications of recycled aggregates: recycled coarse aggregates are most commonly found in aggregate bases, while fines can be utilized for CLSM [5]. Particularly, foam concrete has been shown good potential for using fines [6]. For designing a CLSM material that may introduce recycled fines, a relative proportioning method could be employed to optimize the mix proportions rapidly and systematically [7].

Foam concrete has been broadly accepted in many construction applications because of its untraditional physical properties and functional characteristics, including lightweight, high flowability, self-compacting nature, low thermal conductivity, and fire resistance [8]. At lower densities, foam concrete is usually utilized for filling and insulation purposes [9]. As foam concrete can flow easily under its low self-weight, it is commonly used in filling voids, such as aged sewers, pipes, basements and storage tanks [9]. Foam concrete is also popular for thermal insulation, for example, cavity wall construction [10] and roof-fill insulation [11]. The air entrapped in the foam concrete void system cannot move so that suppressing convective heat transfer to provide thermal insulation [12]. Besides, due to the fire resistance nature of foam, foam concrete is often seen in firewall construction. At higher densities, foam concrete is more adopted as structural elements [9]. Some bridge abutments were constructed with foam concrete, taking advantage of the lightweight and relatively high strength (around 5 N/mm^2) [1]. As such, the imposed lateral load can be reduced [9]; the ground settlement can be minimized [1]; and the bridge foundation size can be decreased [1], [9]. Other applications of foam concrete include road sub-base, soil stabilization, and trench reinstatement [9]. Although foam concrete is restricted from carrying

heavy loads, it possesses many distinctive mechanical characteristics for functional uses in construction.

Foam concrete also shows unique crushing behavior under loading. Compared with solid materials, cellular materials exhibit large deformation and absorb a substantial amount of energy under loading. Analogs of cellular materials in nature are animal bones and plant stems, the function of which widely confirms the effectiveness of cellular structures [13]. Ashby defined three crushing stages for cellular solids during compression: linear-elastic, plateau, and densification [14]. Initially, a cellular solid deforms in a linear-elastic manner; then it reaches to the plateau stage, where the strain increases continuously while the stress remains stable; at the end, the crushed material becomes highly densified such that an instantaneous rise of the stress level is observed [14]. As a result, foam concrete dissipates substantial energy during the crushing process, which makes it an ideal candidate as an energy absorber.

A promising application of foam concrete is used as a runway arresting material for an EMAS. The Federal Aviation Administration (FAA) requires engineered materials to be "high energy absorbing materials of selected strength, which will reliably and predictably deform under the weight of an aircraft" [15]. When an aircraft overrun occurs, the aircraft should be decelerated and finally stopped by rolling and sinking its tires into the engineered materials placed at runway end [16]. With a proper mix design and production, foam concrete could achieve optimal strength for desirable energy absorbing capacity and thus improve the runway safety. Furthermore, the cost of foam concrete material is competitively lower to the commonly used glass foam. Therefore, foam concrete potentially provides an excellent engineering solution for the EMAS application.

There remains much to learn about the behavior of foam concrete. Previous research extensively studied the physical and functional properties of foam concrete, putting the most effort in exploring the applications of volume filling and insulation. In terms of the mechanical property of foam concrete, studies were rather limited. Basic discussion on mechanical properties of foam materials and honeycombs was given by Ashby [17]; some general mechanics and physics of porous solid were provided by Oliver [18]; Roberts analyzed several classes of statistical models which are used to represent porous materials, in order to relate material structure to property [19]. As a result, subjects related to the mechanical behavior of foam concrete are generally less apprehended. Particularly, the relationship has not been well established between the real geometric structure of foam concrete and its actual mechanical behavior. Therefore, it is urgent to acquire better understandings regarding these concerns.

To fill the knowledge gap, it is proposed to start by linking the mechanical responses to the cellular structure on micro level. As such, the investigation focuses on 1) developing a geometric model for foam concrete microstructure based on micro-computed tomography (micro-CT) scan, and 2) conducting a FEM analysis upon this model. Specifically, major steps include: preparing a micro-CT scan, image pre-processing, volumetric mesh generation, and FEM analysis.

2.2 Micro-CT image acquiring

Instead of directly using theoretical geometric models, a micro-CT scan is preferred as the source of foam geometry, in order to be representative of a real-world scenario.

A foam concrete cylinder, with a density of 0.6 g/cc, was prepared using water, cement, foaming agent and superplasticizer. Detailed mixing procedure can be found in the instruction by Song and Lange [20]. A small foam concrete pellet that fit a 5-mm diameter plastic holder was taken from a larger cylinder sample, and further characterized using Xradia MicroXCT-200 CT machine with a voxel resolution of 5 μm [20]. A total of 400 slices were taken, and a slice of the micro-CT scan is shown in Figure 2.2 as an example.

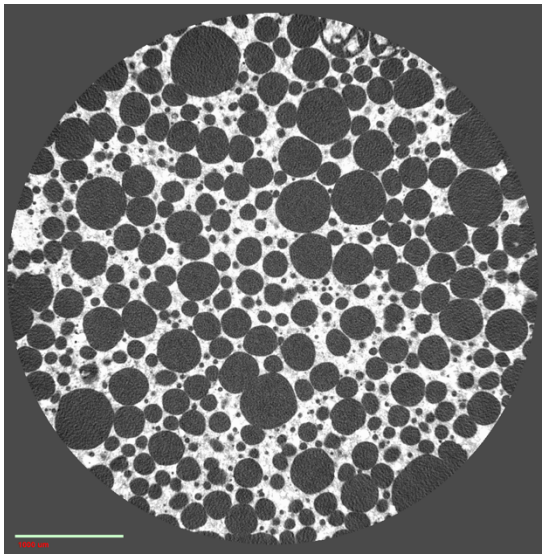

Figure 2.2: A slice of the micro-CT scan of 0.6 g/cc foam concrete. (Credit: J. Clark, UIUC)

The image in Figure 2.2 exhibits a satisfying quality with a good definition and a high contrast. The foam concrete sample contains two main phases, solid paste, and void. The microstructure of the sample is outlined by greyscale in micro-CT scan, where different colors separate the solid and voids. Since the grayscale of the micro-CT scan is counting on the radiation intensity transmitting through the material, darker the color, higher the penetration, indicating lower the material density. It is, therefore, clear that the white color reflects the solid portion of the foam concrete sample, while the black color shows the voids. In the following, the micro-CT scan is processed before fetching a volumetric mesh of foam concrete.

2.3 Image pre-processing

Pre-processing of the raw images was conducted in an open source platform Fiji [21]. The micro-CT scan, with 400 slices numbered in order, were imported into Fiji in sequence and converted to an image stack. As such, each of the following procedures can simply be done to the image stack at one time without repeating for each slice image. Since possible boundary defects could arise in the sample during sample extraction, the image stack was cropped at the center to yield a square area with a 400-pixel (2-mm) side length. Figure 2.3 gives a 3D rendering of the cubic volume.

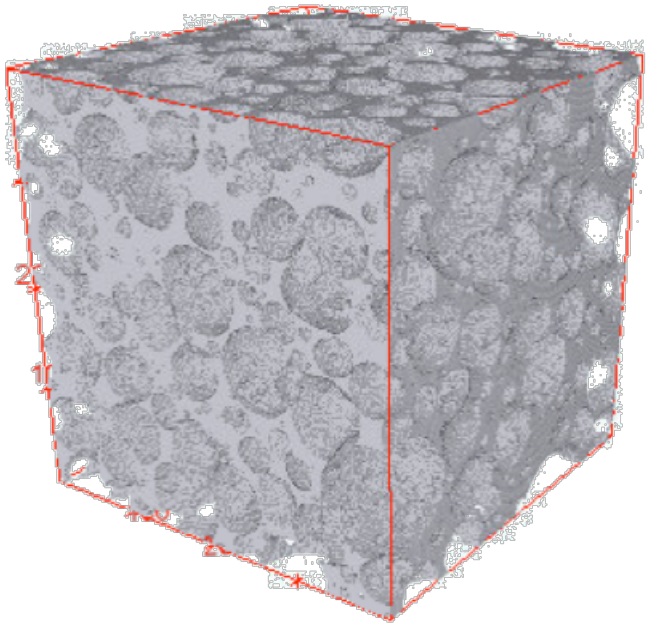

Figure 2.3: 3D volume rendering.

Phase segmentation and image cleaning were the two key steps involved in the image pre-processing. Different shades of grey existed as noises in the micro-CT images. For simplicity, it was assumed that only two phases existed in the microstructure so that binary images were obtained after thresholding. Prior to thresholding, the original image type "RGB color" was switched to "8-bit". Essentially, thresholding is specifying a cut-off value, dividing the original

pixels into two classes according to their pixel values, and assigning a new pixel value (0 for white or 255 for black) to each class [22]. Fiji provides several built-in threshold methods, such as Intermodes, Main, Huang, and Otsu. Among these approaches, Otsu was selected to have a cutoff value of 155 for the image stack, so the pixels lower than that were taken as the white color. As a result, the micro-CT images were converted to binary images. Figure 2.4 shows the Otsu thresholding algorithm. Figure 2.5 compares a slice before and after thresholding.

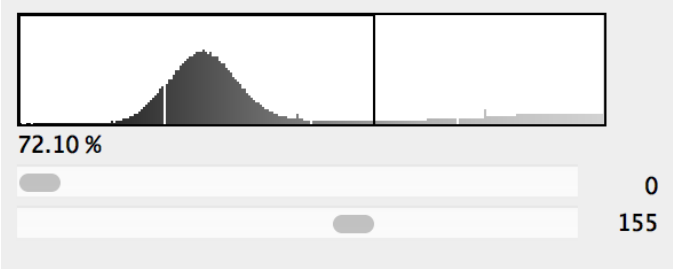

Figure 2.4: Otsu thresholding for the foam concrete micro-CT images.

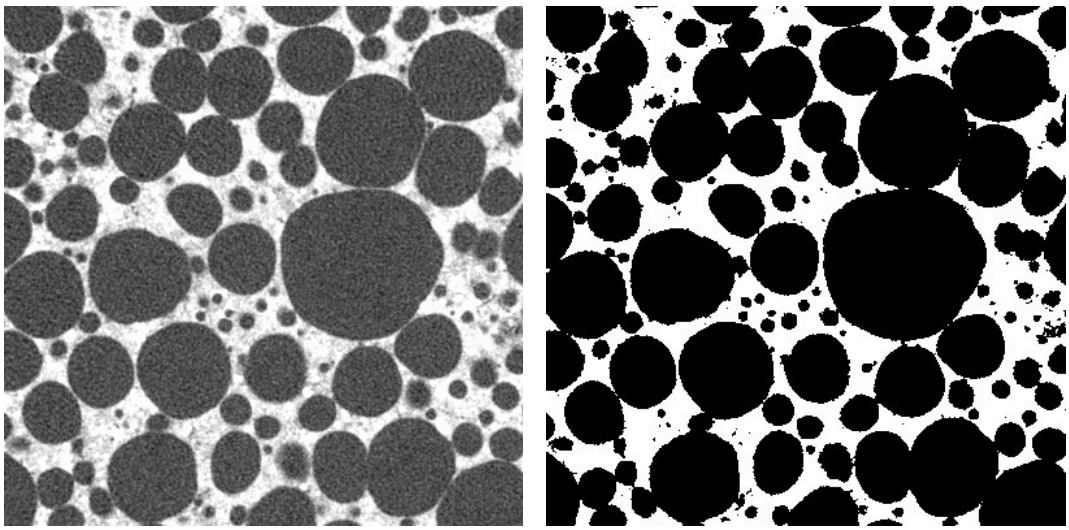

Figure 2.5: A slice of the image stack before (left) and after thresholding (right).

Examining the images after thresholding, small black dots are found scattering over the volume. These dots are possibly the image noises that were brought with the binary conversion, or the small pores in the paste solid. Referring to pore system of autoclaved aerated concrete suggested by Tada

and Nakano [23], microcapillary pores have radii less than 50 nm; macro capillary pores are between 50 nm to 50 μm; and the air pores introduced by surface-active agents range from 50 μm to 500 μm. Assuming the pore system in the foam concrete paste obey the same size distribution, the cellular structure of the foam concrete was built on the air voids larger than 50 μm created by the foam. To focus on the cellular structure reconstruction, the pores and noises that have areas less than a 50-μm circle were removed out in each image. A slice of the cleaned image stack was shown in Figure 2.6(a). In addition, the edges of the pores in Figure 2.6(a) were found a little fuzzy due to limited resolutions. To smooth the pores, an erosion-dilation cycle was performed as shown in Figure 2.6(b). Finally, the smoothed image stack was cleaned twice in order to filter out the remaining noises.

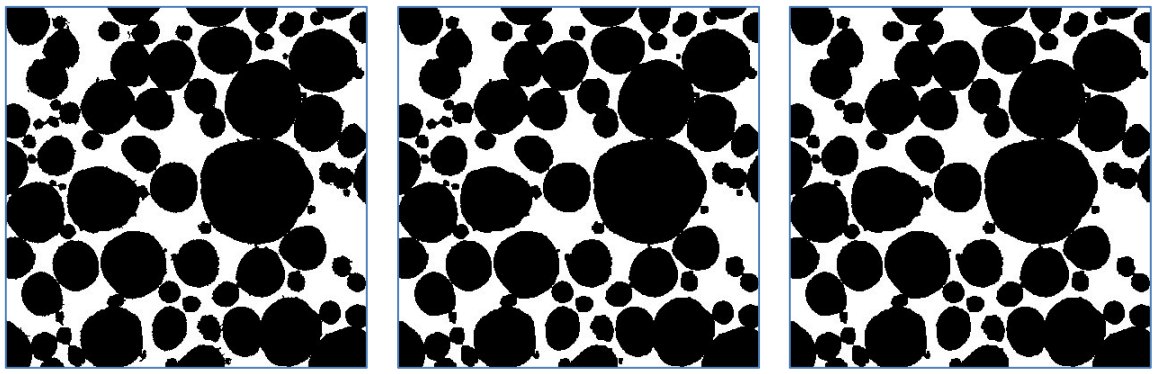

(a) Image after cleaning (b) Image after smoothing (c) Image after 2nd cleaning

Figure 2.6: A slice image after cleaning and smoothing.

From Figure 2.5 to Figure 2.6(c), noises are filtered out and the main structure of foam concrete is retained, resulting in a clearer image with a relative higher quality that could accelerate the meshing generation. However, one possible defect of the processing algorithm is that some information might be lost at the edges. Another defect is some small pores are not filtered when they connect with bigger neighbors, as the processor would consider them as one object with an area greater than the critical value. This defect can be compromised by removing them manually

or splitting them before the cleaning. With the purpose of reducing the meshing error and time, there are several other alternatives in Fiji to attain a satisfying quality as per individual judgment, while details are not illustrated here. In subsequent, the cleaned and smoothed image stack are employed as a geometric basis for reconstructing the foam concrete microstructure.

2.4 Volumetric mesh generation

This section introduces the mesh generation procedure based on the segmented micro-CT images. Since the format of the micro-CT image stack is not compatible with FEM software like Abaqus, creating a mesh in inp. format should be completed before importing into Abaqus.

A MATLAB/octave-based toolbox "iso2mesh" was adopted for creating tetrahedral meshes [24]. This toolbox "iso2mesh" was developed by Dr. Qianqian Fang from Northeastern University based on various open-source meshing tools, in order to achieve an accurate and fast-speed mesh generator for neuroanatomical studies, especially brain atlas. For creating high-quality meshes from volumetric images, the availability of free software or open-source utilities is rather limited, while the commercial packages, such as Amira, Mimics, and Simpleware, are expensive and restricted in functions. In comparison, iso2mesh is more versatile in function and has much higher flexibility by providing access to the original source code.

To generate tetrahedral meshes for the foam concrete microstructure, there are several functions and methods available in iso2mesh. One can design strategies to fulfill a specific purpose. For directly obtaining a tetrahedral mesh from volumetric images, one can use 'vol2mesh' function. Alternatively, one can use a combination of 'vol2surf' and 'surf2mesh' functions to generate a surface mesh and then create a volumetric mesh from the surface. Instead, their shortcuts, 'v2m',

'v2s' and 's2m', can also be used upon preference. In conjunction with the functions, multiple methods with different mesh generating algorithms, such as 'cgalmesh', 'cgalpoly' and 'cgalsurf', are available for varying purposes, or for achieving a satisfying meshing quality within a desirable time.

To evaluate the quality of generated mesh, iso2mesh provides a function 'meshquality' based on Joe-Liu parameter [25]. For each tetrahedron mesh, the Joe-Liu parameter is defined as

$$\eta = \frac{12(3v)^{2/3}}{\sum_{0 \le i < j \le 3} {l_{ij}}^2} \qquad \text{(Eq. 1)}$$

where v is the volume of tetrahedron and l_{ij} is the edge lengths of the tetrahedron [25]. The parameter η falls in the range of 0 and 1, where $\eta = 1$ for a regular tetrahedron and η approaches 0 for a poorly-shaped tetrahedron. If the mesh quality is not desiring, several functions configured in iso2mesh are capable of improving the mesh quality or smoothing the surface mesh, for example, 'sms' or 'smoothsurf".

With the intention of comparison, several volumetric meshes of the foam concrete microstructure were constructed using different functions and methods. The related key code is attached in the Appendix A. Figure 2.7 shows a mesh generated with the 'cgalpoly' method with the 'vol2surf" function. The various colors in this figure denote different locations for better visualization. Firstly, a polyhedral surface was generated from the micro-CT image stack using the method 'cgalpoly'. Then the tetrahedral volumetric mesh was built using the function 'cgals2m' based on the surface mesh. The mesh buildup took about 18 minutes. The final mesh contains 1,078,679 tetrahedrons and 381,926 nodes. Accordingly, the average mesh quality is 0.59, and the histogram of the Joe-Liu metric can also be found in Figure 2.7.

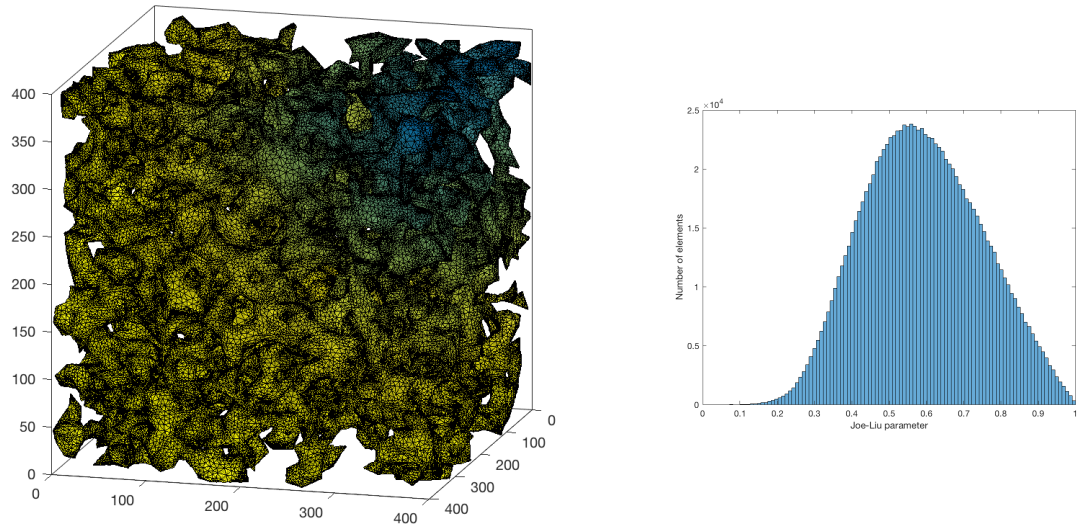

Figure 2.7: Mesh created using ‘cgalpoly’ method and the resultant Joe-Liu metric histogram.

As shown in Figure 2.8, the mesh was constructed with method ‘cgalsurf’ in function ‘vol2surf’ and function ‘surf2mesh’. The method ‘cgalsurf’ used CGAL mesher to generate a surface mesh from the volumetric images. In subsequent, function ‘surf2mesh’ was applied to build a tetrahedral mesh from the closed surface. The final mesh contains 1,747,524 tetrahedrons and 448,157 nodes in total. The corresponding average mesh quality is 0.74.

Figure 2.9 shows the volumetric mesh directly created with method ‘cgalmesh’ in function ‘vol2mesh’. A total of 2,300,782 tetrahedrons and 749,465 nodes were generated within 6 minutes with an average mesh quality of 0.62.

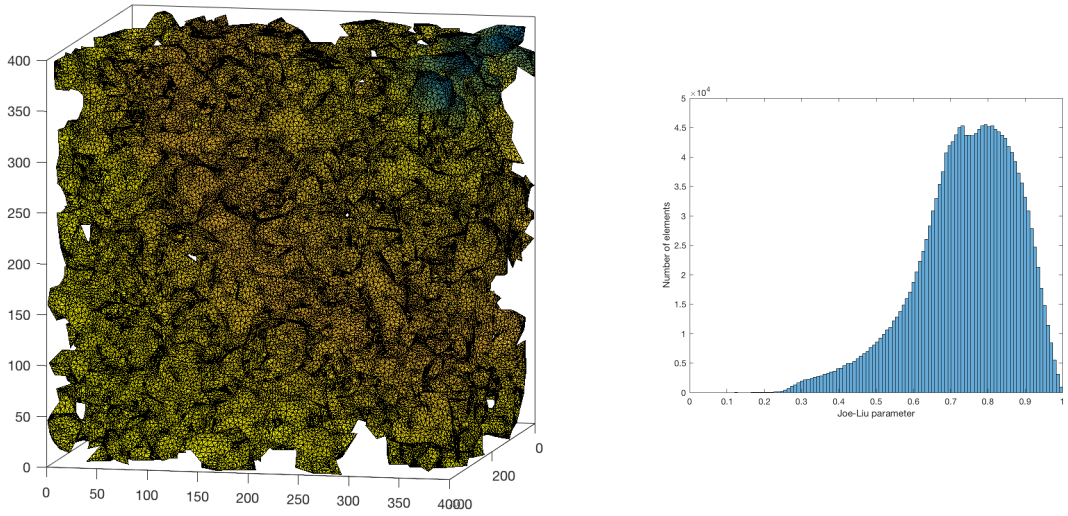

Figure 2.8: Mesh created using ‘cgalsurf’ method and corresponding Joe-Liu metric histogram.

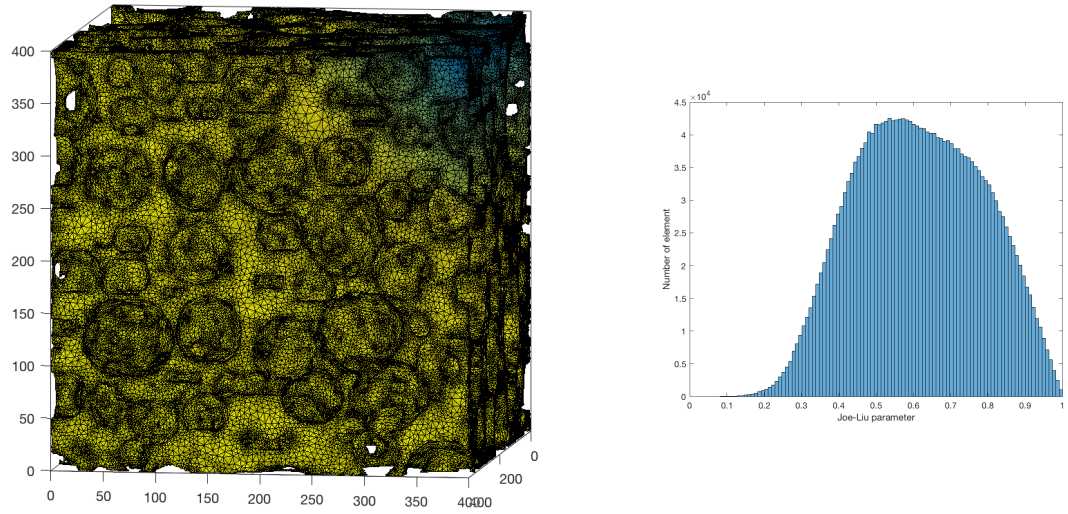

Figure 2.9: Mesh created using ‘cgalmesh’ method and the resultant Joe-Liu metric histogram.

Comparisons are made among the meshes created with different meshing algorithms. Using the average Joe-Liu parameter to evaluate the mesh quality, method ‘cgalsurf’ is found superior to ‘cgalmesh’ and ‘cgalpoly’. As shown in Figure 2.8, the Joe-Liu values of the mesh created with ‘cgalsurf’ method are concentrated in the range between 0.7 and 0.9, resulting in an average of 0.74. As for the mesh created with method ‘cgalpoly’ in Figure 2.7, the Joe-Liu parameters fall in

0.5-0.7, with an average being 0.59. Thus, ‘cgalsurf’ is preferred than ‘cgalpoly’. Another observation also supports the method ‘cgalsurf’ as the resultant mesh in Figure 2.8 contains elements 38% greater than the ‘cgalpoly’ mesh in Figure 2.7. In addition, as compared to the mesh in Figure 2.7, the mesh in Figure 2.8 is smoother and restores more accurate microstructure of foam concrete, which further validates that ‘cgalsurf’ is over ‘cgalpoly’.

However, for comparing ‘cgalsurf’ and ‘cgalmesh’, the observations from the mesh plots and the element numbers contradict with the indication from the Joe-Liu mesh quality parameter. According to the histogram in Figure 2.9, the Joe-Liu values distribute mainly in 0.4-0.8, with an average of 0.62, which is lower than that of the mesh in Figure 2.8. The average Joe-Liu parameter suggests ‘cgalsurf’ is more accurate than ‘cgalmesh’. However, the mesh elements in Figure 2.9 is 24% more than that in Figure 2.7. Furthermore, Figure 2.8 shows a rather well-defined microstructure of foam concrete with a smooth surface and detailed air void configuration. Therefore, average Joe-Liu parameter cannot simply be taken as the only criteria in evaluating the mesh quality. Other factors like element number and mesh plot should also be analyzed in order to provide a comprehensive assessment of the mesh quality. In this case, the method ‘cgalmesh’ is considered robust and preferable than ‘cgalsurf’ and is adopted.

For reducing the computational cost in FEM analysis, the model size was reduced to a 1-mm cube. The volumetric mesh of the foam microstructure was created using ‘cgalmesh’ method as shown in Figure 2.10, which contains a total of 317,958 elements and 105,609 nodes. The microstructure and pore geometry are well restored. Besides, the mesh is smooth and well-defined. With the mesh satisfied, the mesh is exported to an inp. file for FEM analysis.

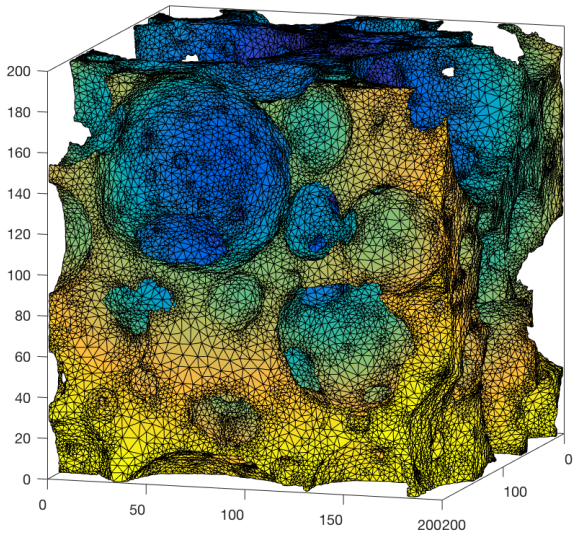

Figure 2.10: The volumetric mesh of a 1-mm cube foam concrete.

2.5 Finite element analysis

A preliminary FEM analysis of foam concrete microstructure was conducted using the volumetric mesh. The analysis mainly focused on the providing a preliminary understanding of the stress response of foam concrete under uniaxial deformation. For this purpose, a qualitative analysis was implemented with a FEM software Abaqus/CAE. Generally, a complete FEM simulation in Abaqus/CAE is comprised of geometry construction, mesh generation, material property assignment, boundary condition confinement, loading, and computer calculation. As the geometry construction and mesh generation have been completed in iso2mesh, this work focuses on the remaining steps.

Prior to assigning the material properties, the volumetric mesh shown in Figure 2.10 was imported into Abaqus/CAE with an element type of C3D4, i.e., 4-node linear tetrahedral elements. The success of importing the mesh validates the compatibility with Abaqus/CAE.

The previous assumption indicates the foam concrete sample in the study contains only two phases. As the solid phase is restored in the volumetric mesh model, cement paste in the foam concrete sample is studied. To simplify the problem, the solid material is assumed behaving only in a linear elastic manner. Based on typical engineering practices, the density, elastic modulus, and Poisson's ratio of cement paste were assigned to reasonable values as tabulated in Table 2.1.

Table 2.1: Material property of cement paste

Material	Density (kg/m^3)	Elastic modulus (Pa)	Poisson's ratio
Cement paste	2000	2×10^{10}	0.3

The boundary condition of the foam concrete model was assigned as the next step. To obtain the foam concrete stress response under deformation, a uniaxial compression simulation was carried out to simplify the problem. To simulate a uniaxial compression test in Abaqus/CAE, the foam concrete model was fixed on the bottom and a vertical displacement was prescribed from the top. Viewing the model from the side as shown in Figure 2.11, elements on the bottom layer of the foam concrete were restrained in all directions to provide a fixed condition, while elements on the top layer were assigned a downward displacement that the foam concrete was compressed with a constant rate.

As for the loading condition, only the foam concrete self-weight was considered. Static stress and displacement analyses were implemented using "Static, general" procedure in Abaqus/Standard, as a commonly used implicit solver. The large-displacement formulation was activated in this solver to handle potential nonlinear effect that might occur during the simulation.

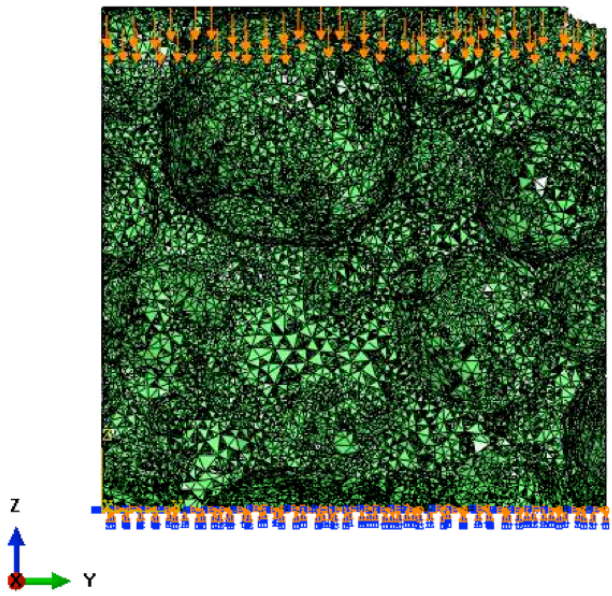

Figure 2.11: Boundary condition on foam concrete model.

Figure 2.12-2.16 give the structure stress response in a progressive manner. In particular, Figure 2.12 demonstrates the initial state of foam concrete without stress concentration, while Figure 2.16 illustrates the stress response of foam concrete in 3D (left) and 2D (right) at the end of the deforming process. The 3D and 2D microstructure stress response at 1/4, 1/2, and 3/4 of the total deformation length are shown in Figure 2.13-2.15, respectively. In these figures, different colors indicate different stress levels, where warmer color indicates greater stress intensity.

In Figure 2.13, stress development is initiated as manifested by the presence of green color on the microstructure. The stress first builds up from the thinner cell walls, which are usually weaker in foam concrete microstructure. The phenomenon is expected as it is in accordance with the understanding of stress concentration. With the deformation process going, the stress develops as the influencing area spreads out, as shown in Figure 2.14. Figure 2.15 shows the stress distribution at halfway during the deformation process. Compared to the previous stage, the stress

concentration has broader influences over the volume, together with the stress on cell walls rises to higher levels. In addition, the pore structures in Figure 2.15 are more distorted to some extent under the prescribed compressive displacement. In Figure 2.16, the microstructure is highly deformed, and the stress concentration is extensively distributed over the volume.

From Figure 2.12 to 2.16, the stress builds up as the foam deformed, and the stress distribution is qualitatively reasonable. This observation indicates a potential for characterizing the foam concrete behavior on micro level. However, there are some limitations involved in the FEM simulation. One limitation lies in the material model. As to simplify the problem, it was assumed that foam concrete is a linear-elastic material and no material failure would occur. To provide a more realistic prediction, a material failure model should be applied in conjunction with elastic properties. Additionally, the analysis of foam concrete micromechanical behavior stayed at a qualitative stage. After obtaining a reliable model, quantitative analyses can be performed in subsequent to investigate the stress-strain constitutive of the cellular structure.

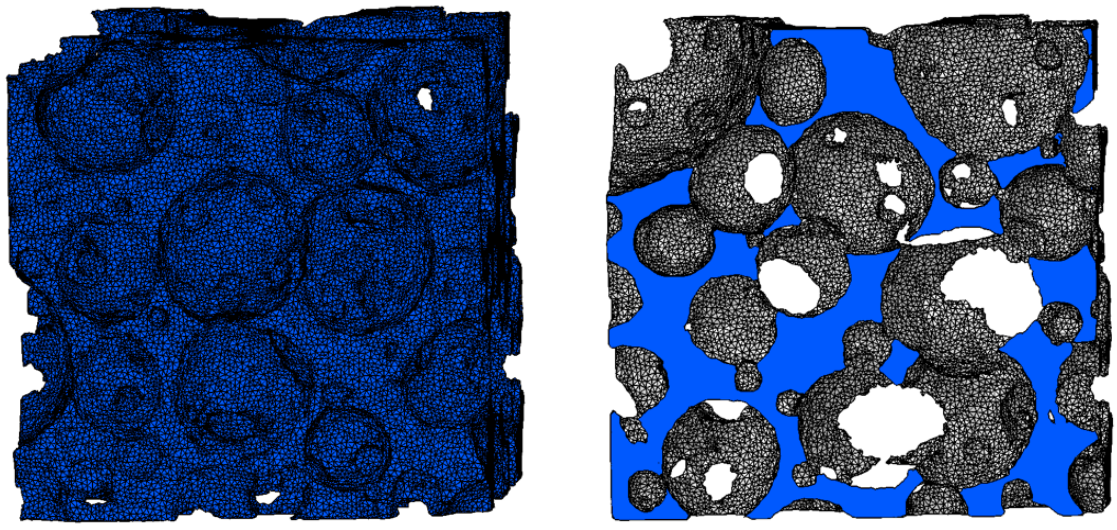

Figure 2.12: Stress distribution in 3D (left) and 2D (right) at the initial state.

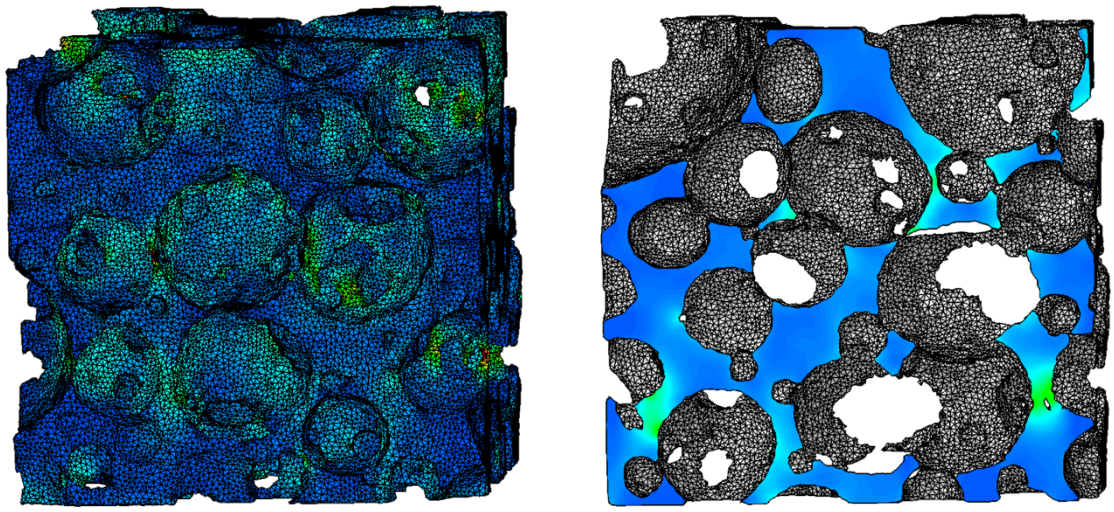

Figure 2.13: Stress distribution in 3D (left) and 2D (right) at 1/4 of the total deformation length.

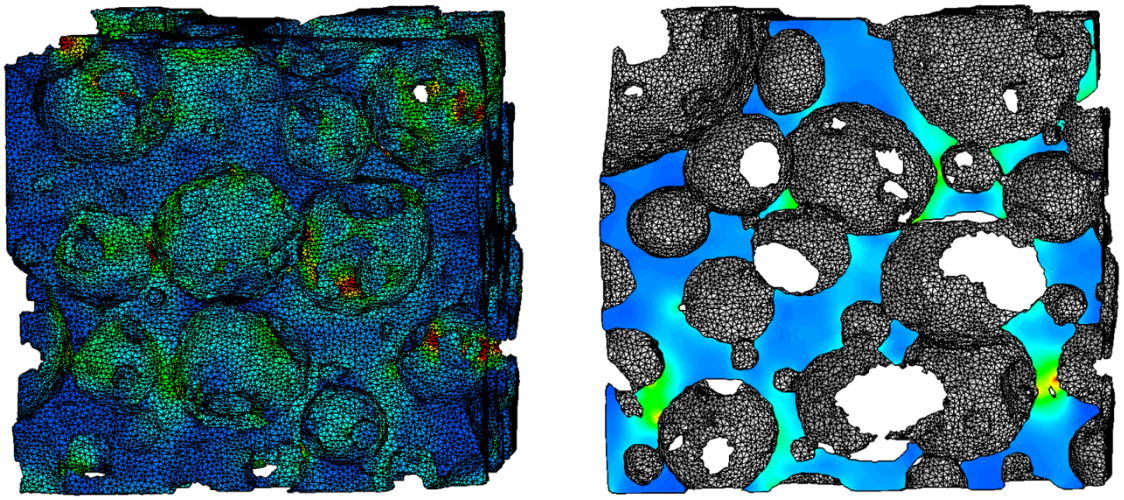

Figure 2.14: Stress distribution in 3D (left) and 2D (right) at half of the total deformation length.

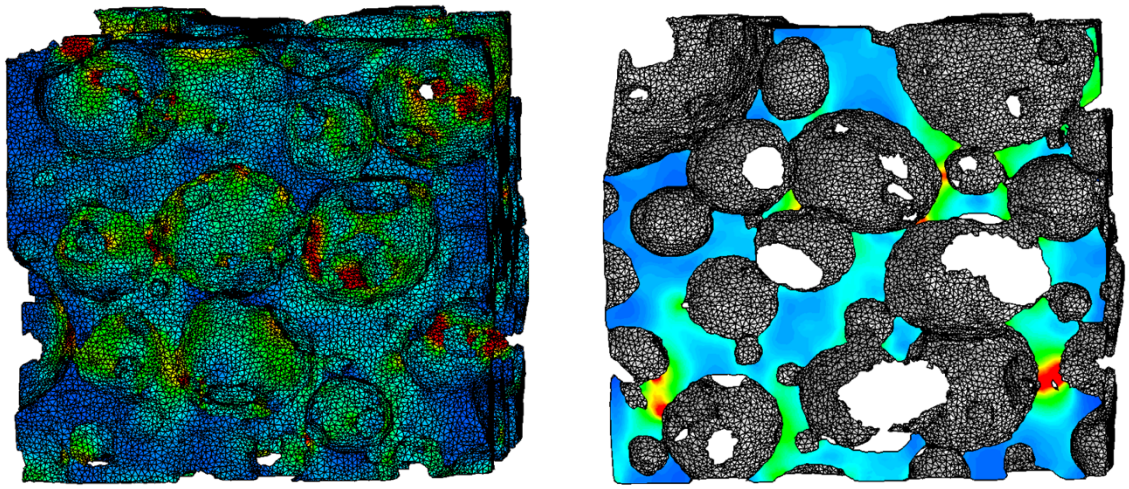

Figure 2.15: Stress distribution in 3D (left) and 2D (right) at 3/4 of the total deformation length.

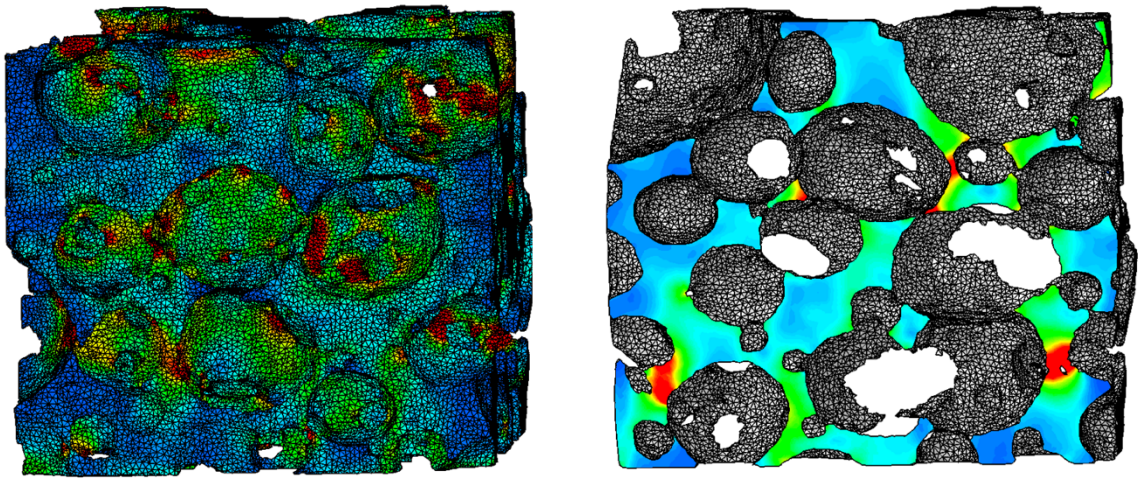

Figure 2.16: Stress on foam concrete in 3D (left) and 2D (right) at the end of the deformation

CHAPTER 3: FINITE ELEMENT MODELING OF AIRPORT SLAB MOVEMENT

3.1. Introduction

Chicago O'Hare International Airport (ORD) uses a tunnel at Terminal 1 as a secure walkway connecting B and C concourses. Figure 3.1 shows the tunnel boundaries defined on a Google Earth image. A continuing liquid leakage problem has been found in the tunnel, as a result of water and deicers running off from the surface of apron and taxi lane. The leakage problem is suspected to be induced by the slab movement between concourses B and C. The slab movement can cause stress buildup near the tunnel, which may further result in damage of the tunnel structure and lead to the leakage. Concrete edge breakage, which is usually associated with high contact stress between slabs, was observed as shown in Figure 3.2.

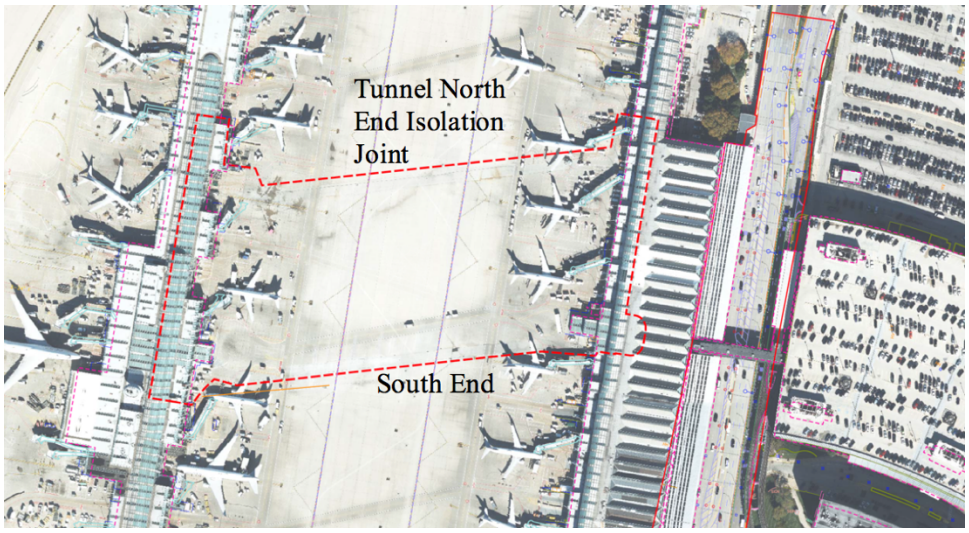

Figure 3.1: Tunnel boundaries defined on Google Earth image.

Field observations suggest that the slab movement is influenced by temperature changes. The expansion joint near the tunnel opens and closes from one season to the next by up to two inches.

Extended periods of hot weather or soaring summer temperatures may cause a complete shutting of the joint, while cold winter temperatures seem associated with joint opening.

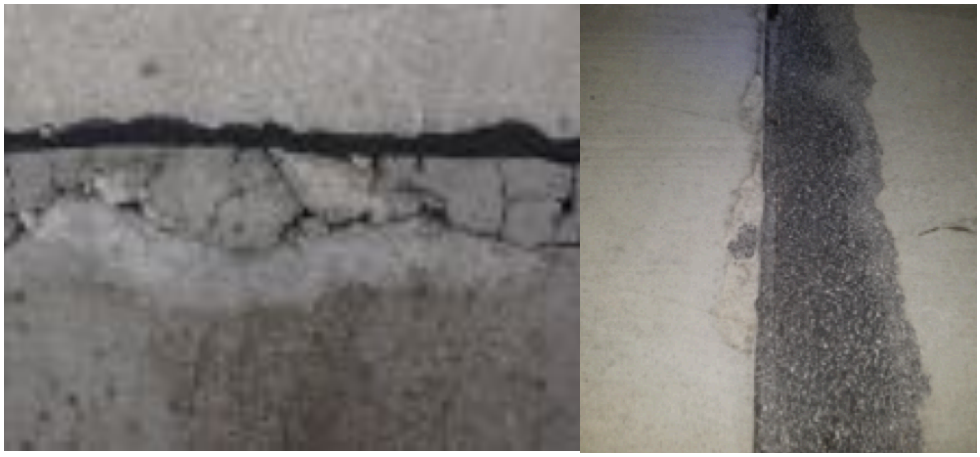

Figure 3.2: Edge breakage at joints

In this study, FEM simulation is conducted to investigate the slab movement under the thermal influence. The major tasks are to simulate change of the joint opening and to estimate stress level in the slabs. Four model configurations are proposed for the full-scale slabs to estimate the opening at concrete expansion joints. Comparison between the simulation results and the field measurement is made to evaluate the model performance. Influence of the expansion joint width on the stress buildup in the tunnel is investigated to provide insights for the subsequent repair works.

In the FEM analysis, the concrete slabs paved between the two concourses B and C are considered as the region of interest. The simulation is conducted in Abaqus/CAE with the following major steps: 1) construct the geometry of the interested region, 2) assign material property and define boundary condition, 3) apply thermal changes, and 4) output the displacement and stress results.

3.2. Basic model configuration and analysis

At the beginning, a FEM model with simplified assumptions is built to serve as the basic model for this study. The configuration of the basic model, including geometry, material property, meshing scheme, boundary conditions are elaborated in the following.

The 3D geometry of the region of interest was constructed using AutoCAD. A satellite photo from Google Earth was used as the reference during this process, which is shown in Figure 3.3. The individual concrete slabs were outlined as single units during the geometry construction. The typical size of a slab unit was approximately 7.6 m by 7.6 m (25 ft by 25 ft). Depth of slab was assumed to be 1/20 of the side length, i.e. 0.38 m (1.25 ft). The structures including Concourse B, Concourse C, and B-C tunnel were considered as the boundary. The constructed geometry is shown in Figure 3.4, where the slab units were sketched as blue grids and the boundary was highlighted with red color.

Figure 3.3: A satellite image of the interested region from Google Earth.

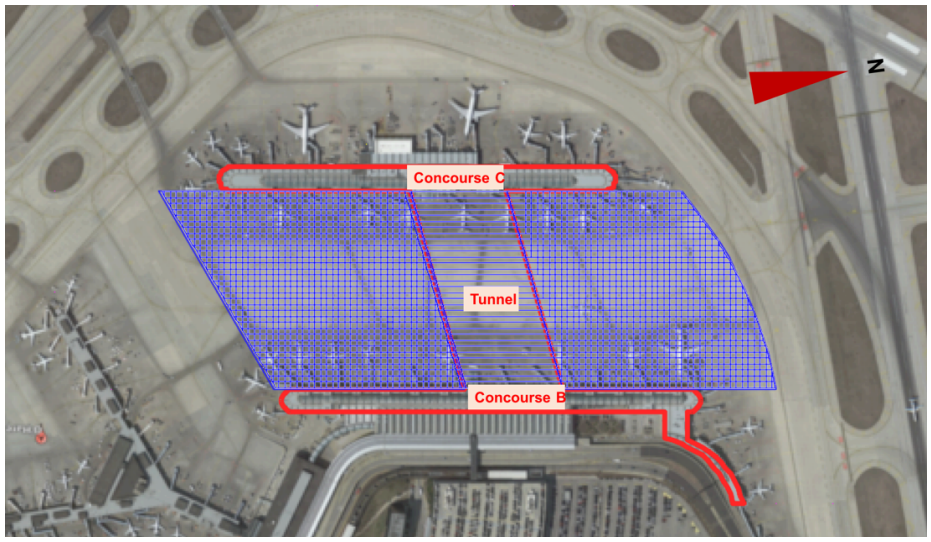

Figure 3.4: Constructed geometry of the basic model.

To avoid unnecessary complexity during the modeling work, a simplified geometry was prepared in Figure 3.5. Since most slab units were tied by dowel bars, the individual small slab units were replaced with two large parts as separated by the B-C tunnel. In Abaqus/CAE, the two major concrete slabs were assigned to be 3D deformable solid, while the boundary structures were assigned to be rigid body due to rigidity difference. Besides, a rigid base was modeled to incorporate friction into the simulation. The slab model was laid on the X-Y plane in Abaqus/CAE.

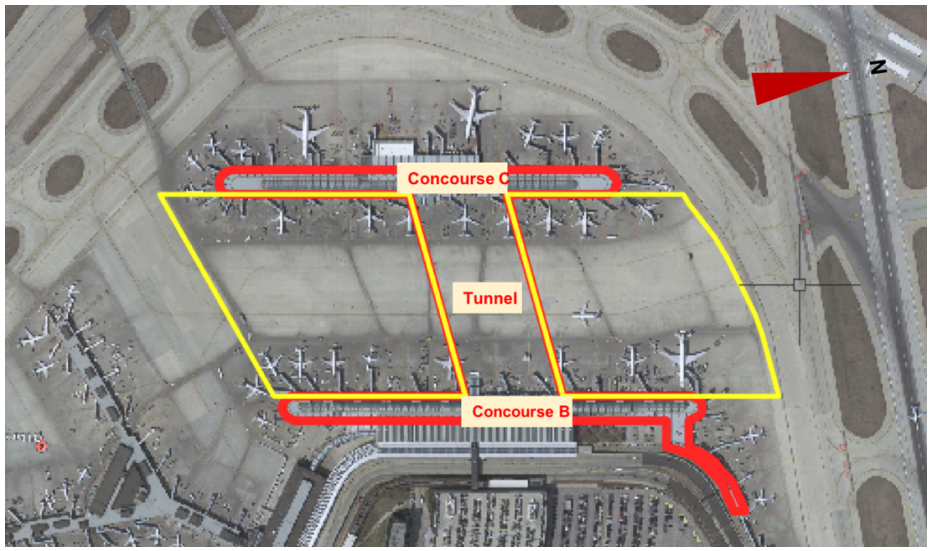

Figure 3.5: Simplified geometry for the basic model.

The concrete material was assumed to have a single thermal expansion coefficient, as the thermal change could only induce small deformation in concrete. The nonlinear material behavior of concrete under large deformation was not considered. Based on typical engineering practice, the material properties of concrete used for the modeling are shown in Table 3.1 [26], [27].

Table 3.1: Material property of concrete

Material properties	Concrete
Density (kg/m^3)	2400
Elastic modulus (GPa)	40
Poisson's ratio	0.15
Expansion coefficient (/ºC)	1E-5

Different element types were selected for the slabs and for the rigid parts. An 8-node linear deformable brick element, C3D8, was used to model the concrete slabs. This solid element has 3 degrees of freedom at each of its 8 nodes. Thus, the slabs were allowed to move freely in X, Y, and Z directions, but not to rotate. A 4-node 3D bilinear rigid quadrilateral element, R3D4, was used to model the base and the other rigid parts. The initial trails found that using a finer mesh in the model resulted in higher accuracy at the cost of computational time. Therefore, a balance between mesh density and computational cost was made to optimize the overall simulation performance. For the deformable parts, i.e. concrete slabs, the mesh was assigned finer to increase the accuracy. An example of the FEM model is shown in Figure 3.6, where 7452 elements were used for the concrete slabs, 2880 elements were used for boundary structures, and 4302 elements were used for modeling the base.

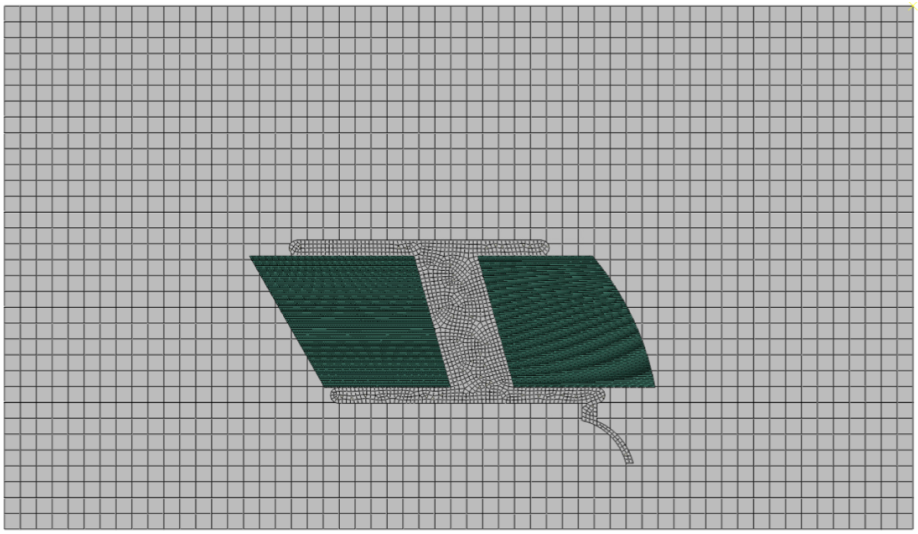

Figure 3.6: A finite element meshing example of the basic model.

The base and the boundary structure assumed to be rigid were fixed in place. During the simulation, movement of the concrete slabs were restrained by these fixed boundaries. A "hard contact" mode in Abaqus/CAE was used to simulate the interactions between the slabs and the rigid boundaries, as shown in Figure 3.7. As such, the contact pressure was transferred only when they are in physical touch. No friction was assumed in the contact interface, but a reasonable Coulomb friction coefficient of 0.3 was assigned to the base. The self-weight of the concrete slabs was implemented.

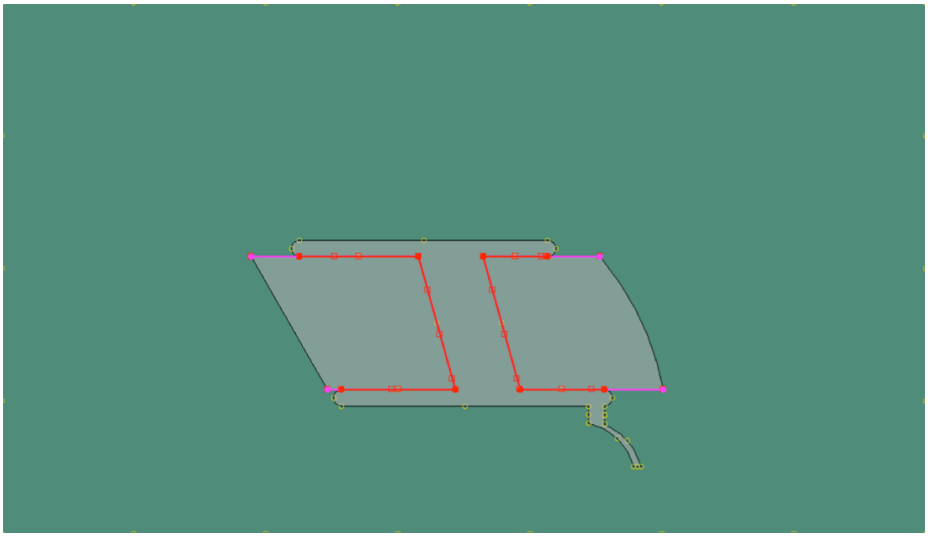

Figure 3.7: "Hard contact" between the slabs and the rigid boundaries.

The temperature variation in the model was fulfilled by using different temperatures during different stages of the simulation. Two thermal steps were implemented to accomplish a complete temperature cycle of 20 ºC. The initial temperature was set to -5 ºC. The temperature after step 1 was set to 15 ºC to render an equivalent temperature rise of 20 ºC. After step 2, the temperature was set back to -5 ºC. With such a configuration, the interaction between the slabs and the boundary was simulated due to the slab expansion during temperature rise, and the thermal stress could be eliminated at the end of the simulation. Static stress and displacement analyses were output from each step using "Static, general" procedure. The large-displacement formulation was activated in this solver to handle potential nonlinear effect that might occur during the simulation. The out-of-plane response in Z direction was not considered in this analysis.

The outputs of slab deformation and stress distribution of the basic model are given in Figure 3.8 to 3.13, in which from left to right present the model responses at the initial temperature of -5 ºC, the peak temperature of 15 ºC (slab expansion), and the ending temperature back to -5 ºC (slab contraction). In addition, the visual presentation of the slab deformation is magnified by a scale factor of 200.

During the temperature rise, the slabs expand outward, and the degree of displacement increases from inside to outside, as reflected by the color pattern of the displacement shown in Figure 3.8. When temperature returns to the initial stage, the slabs contract inward while small openings near the tunnel are observed. This should be attributed to the effect of the base friction on the slab movement. The friction should result in a small amount of constraint to the motion such that the slabs cannot be expanded or contracted in an ideal way.

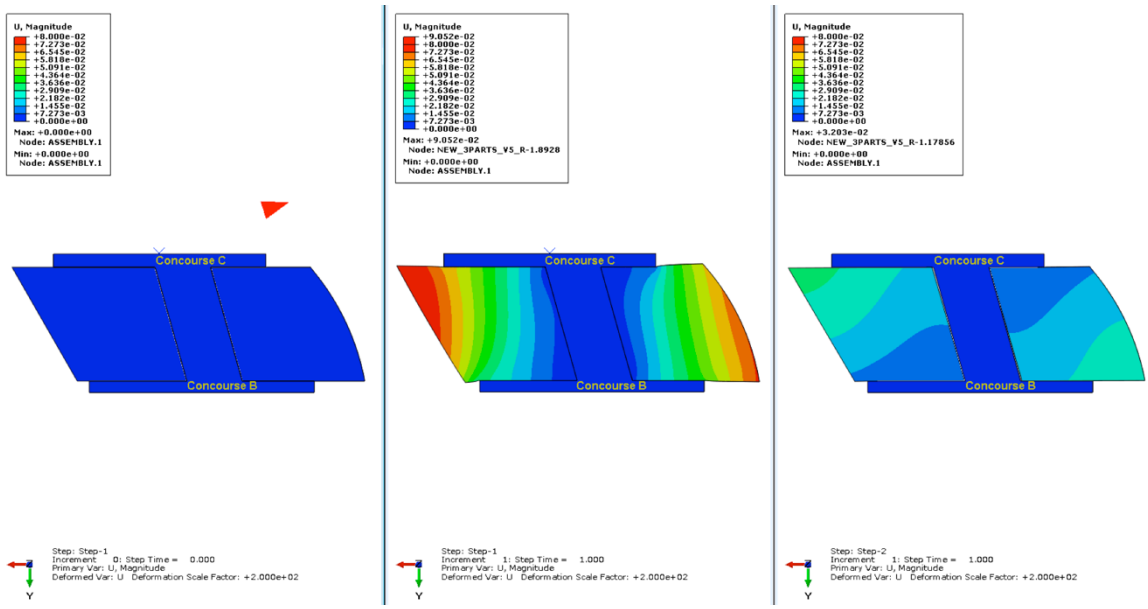

Figure 3.8: Displacement of slabs in the basic model, by m.
(left: -5 ºC center: 15 ºC right: -5 ºC)

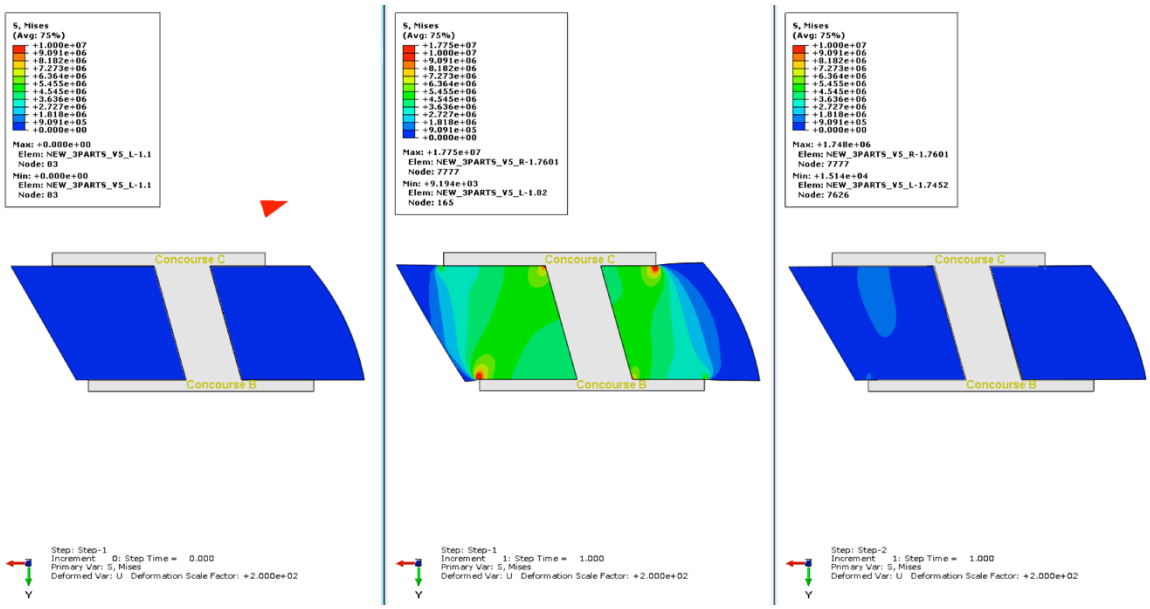

Figure 3.9: Effective stress distribution of slabs in the basic model, by Pa.
(left: -5 ºC center: 15 ºC right: -5 ºC)

The distribution of effective stress is shown in Figure 3.9. After the slab expansion at 15 ºC, the stress is concentrated at the inner corners next to the tunnel; the stress near the free edges is

negligible. At the end of the simulation, residual stress is observed on the slabs, which further confirms the influence of base friction.

For normal stress presented in Figure 3.10 and 3.11, the positive tensile stress is indicated in red, and the negative compressive stress is in blue. Comparing these two figures, it was found that the normal stress in Y direction is higher and it has a larger coverage area than the normal stress in X direction. This phenomenon is expected as the concrete slabs are more confined in Y direction in this model. Overall the outputs from the basic model are found to be reasonable. The basic model is then further modified to incorporate other influencing factors into the simulation.

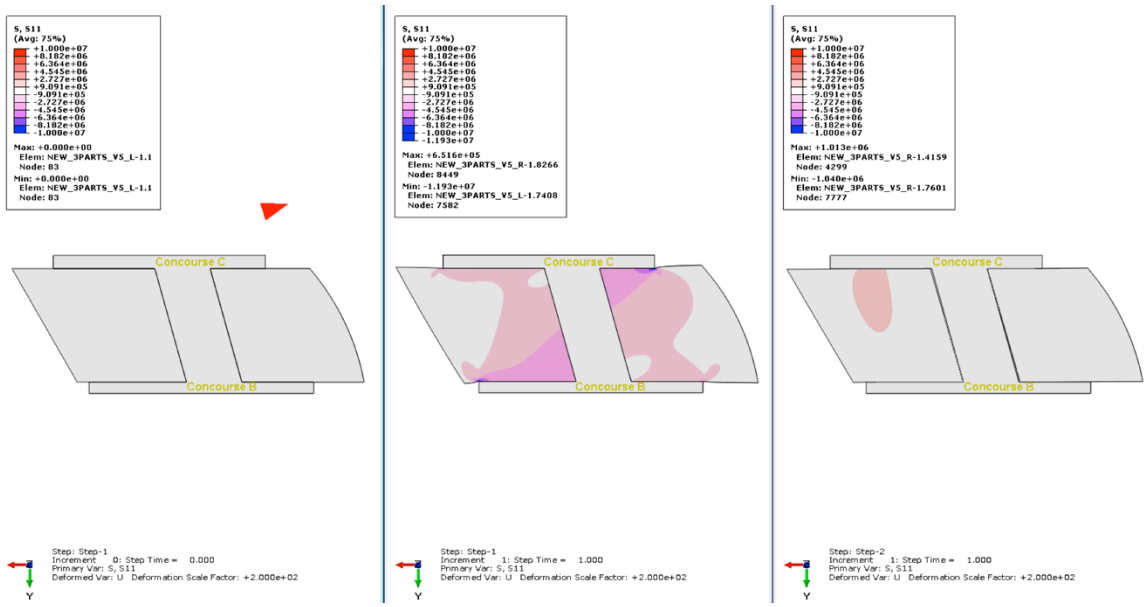

Figure 3.10: Normal stress of slabs in X direction in the basic model, by Pa.
(left: -5 ºC center: 15 ºC right: -5 ºC)

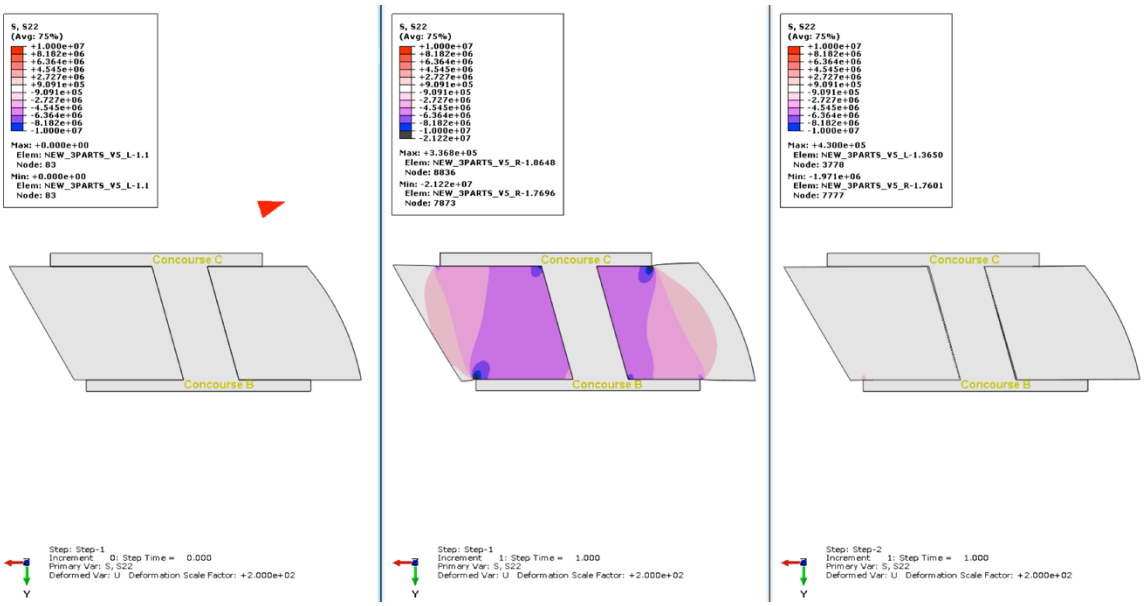

Figure 3.11: Normal stress of slabs in Y direction in the basic model, by Pa.
(left: -5 ºC center: 15 ºC right: -5 ºC)

3.3 Inclusion of utility vaults

As the next step, special attention is given to the utility vaults on the concrete slabs, as shown in Figure 3.12. As these holes act as fixed points on the slabs, the induced constraint is expected to have a strong influence on the overall response of the slab movement and the stress distribution. Therefore, a model including utility vaults is investigated. Figure 3.13 shows the configuration.

Compared with the basic model from the previous section, holes with the same locations and sizes of the utility vaults were updated to the basic model, as presented in Figure 3.13. The utility vaults, as highlighted by yellow dots, were set as fixed boundaries in which any movement was prohibited. To investigate the accumulated effect of slab movement, two temperature cycles were simulated. For each cycle, the temperature started from -5 ºC to 15 ºC and then returned to -5 ºC.

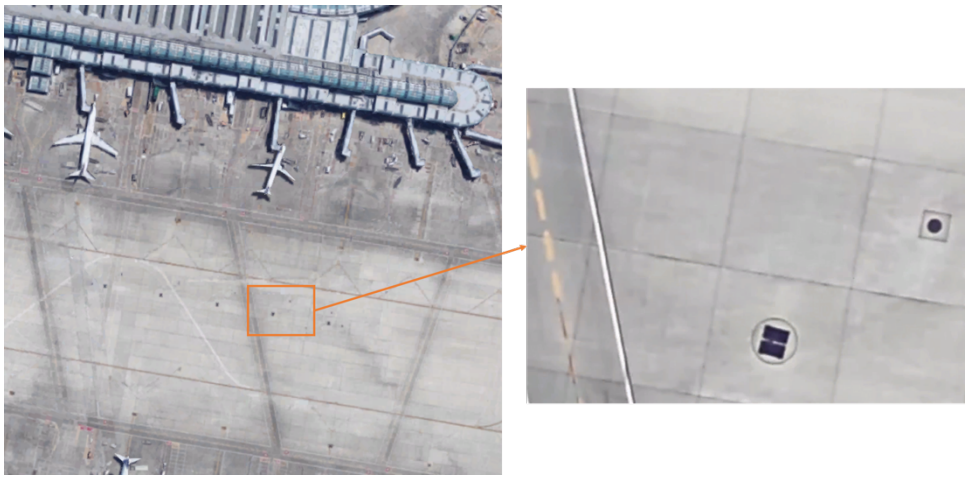

Figure 3.12: Utility vaults on the concrete slabs.

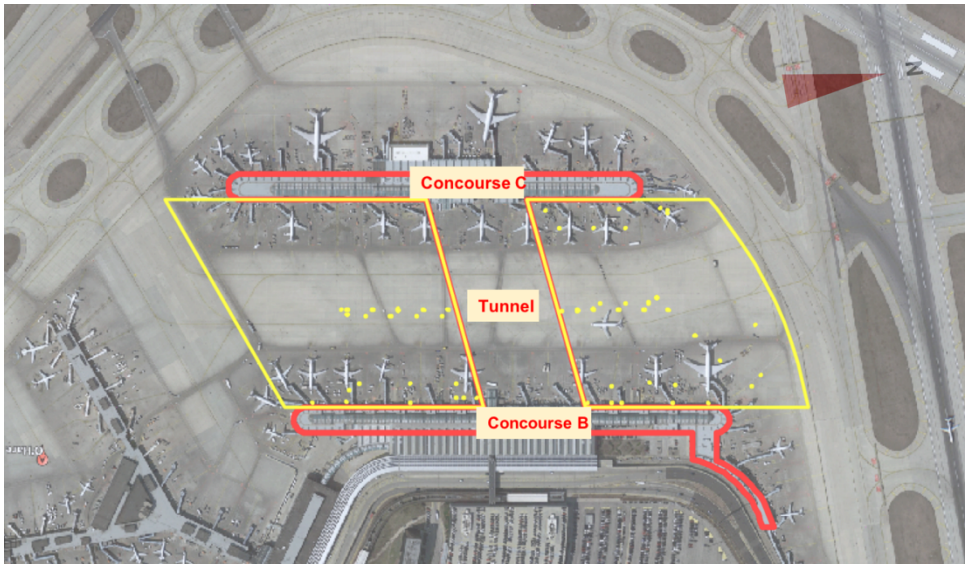

Figure 3.13: Geometry of model including utility vaults.

The outputs of slab deformation and stress distribution of the model with the utility vaults are given in Figure 3.14 to 3.17. In comparison to Figure 3.8, the displacement shown in Figure 3.14 suggests zero displacement near the utility vaults, but the overall displacement response follows the same trending as discussed earlier. After contraction, the opening near the tunnel is observed again. Comparing the degree of the maximum opening along the inner boundary between the two

complete temperature cycles, the displacement accumulation is 0.02 mm. This accumulated effect is so small that it would not impose an evident influence on the slab movement.

As for the effective stress shown in Figure 3.15, the highest stress is found to concentrate at not only the inner corners of the slabs but also near the utility vaults. For the normal stress in X direction shown in Figure 3.16, stress concentration is found near the utility vaults. The slab expansion is largely restrained by the "fixed points". As for the normal stress distribution in Y direction shown in Figure 3.17, only compressive stress is observed because the movement in Y direction is not constrained by the utility vaults. Comparing all the stress results as given in Figure 3.15 to 3.17, the stress level is found to be slightly higher at the second temperature cycle, but the overall differences of stress distribution between the two temperature cycles are insignificant.

Overall, the induced constraints from the utility vaults have a strong influence on the slab movement and the stress distribution. The accumulated effect after the first cycle is found to be insignificant. Therefore, only one thermal cycle is used for further analysis.

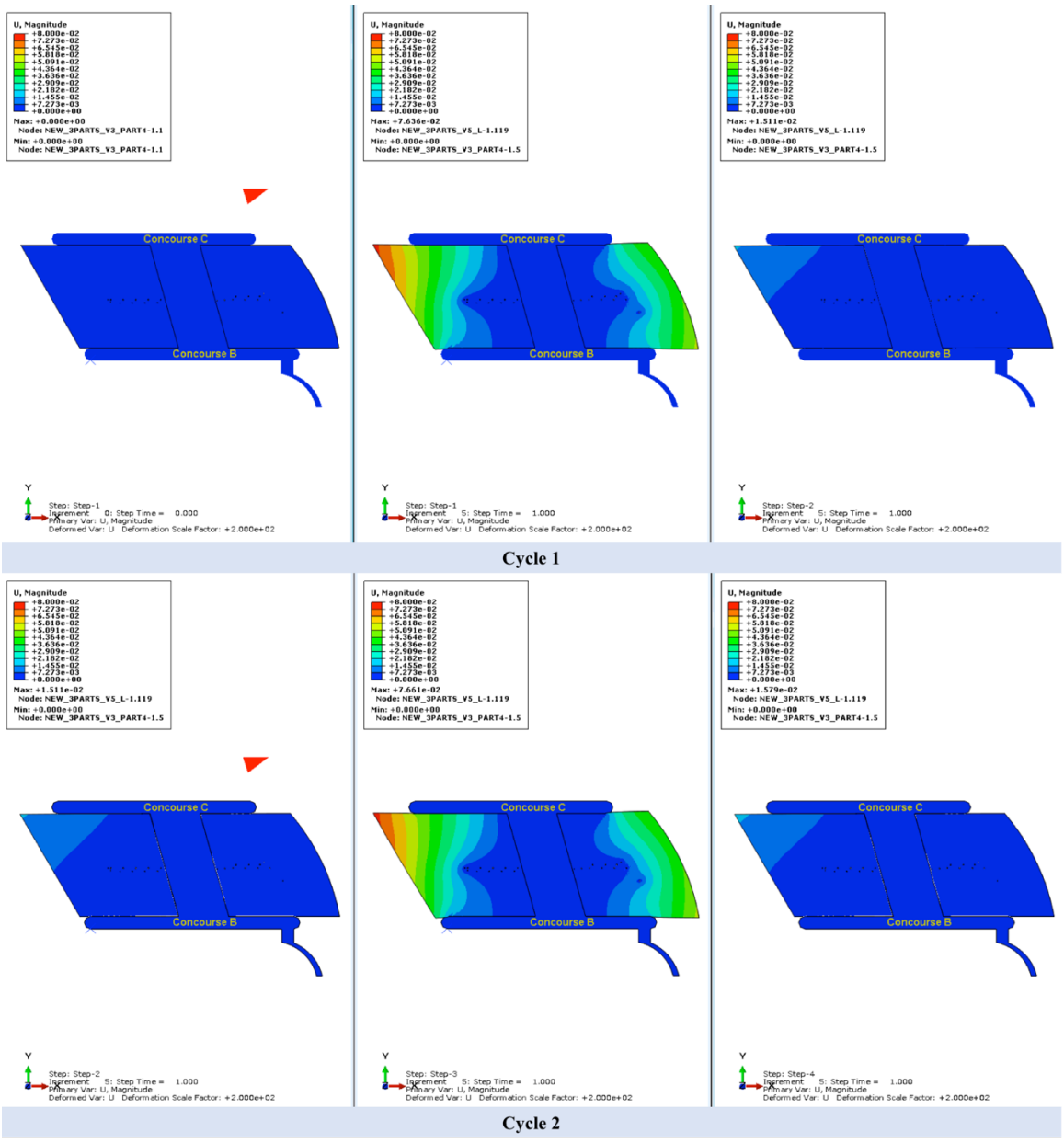

Figure 3.14: Displacement of slabs in the model with utility vaults, by m.
(left: -5 ºC center: 15 ºC right: -5 ºC)

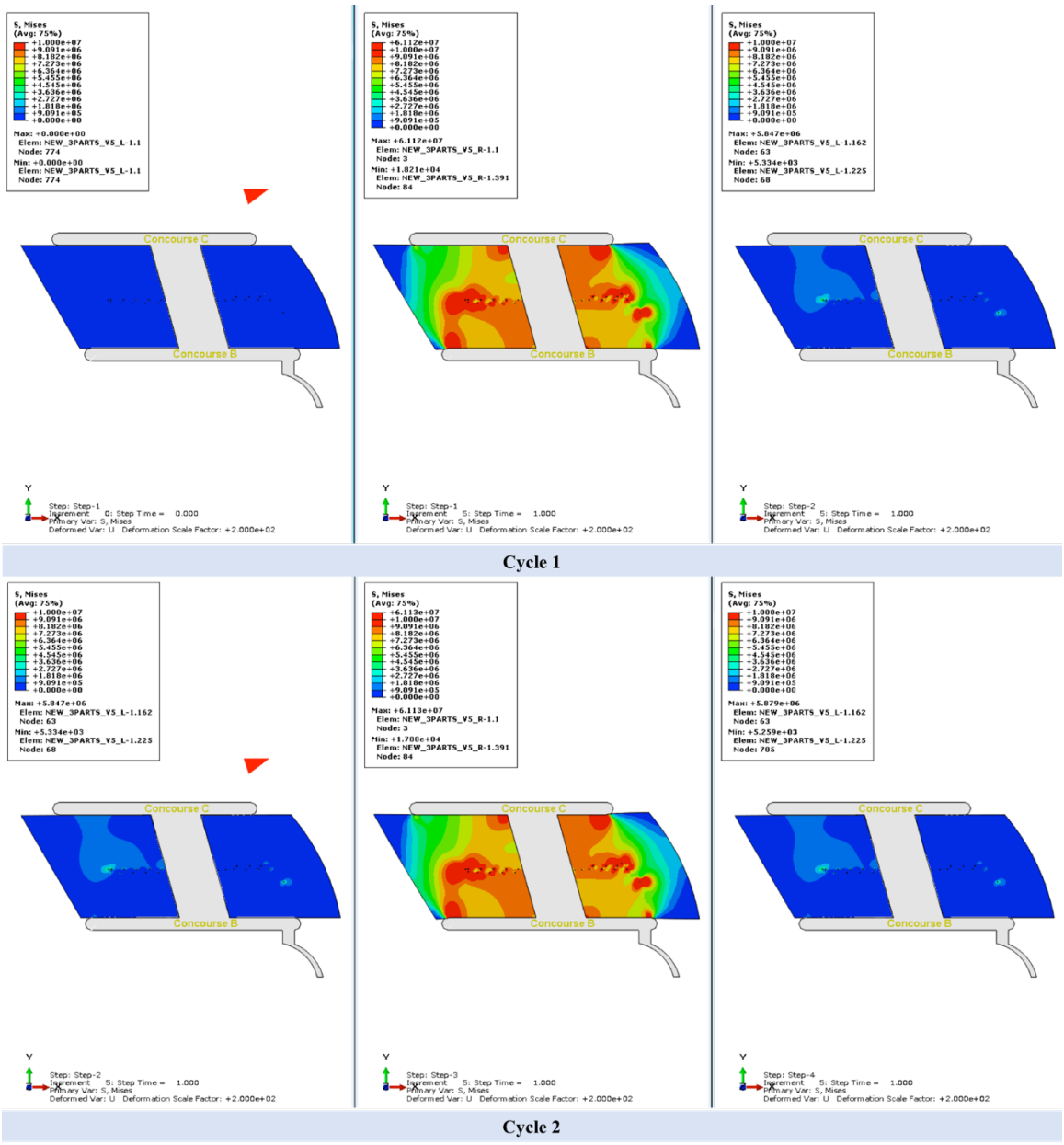

Figure 3.15: Effective stress distribution of slabs in the model with utility vaults, by Pa. (left: -5 ºC center: 15 ºC right: -5 ºC)

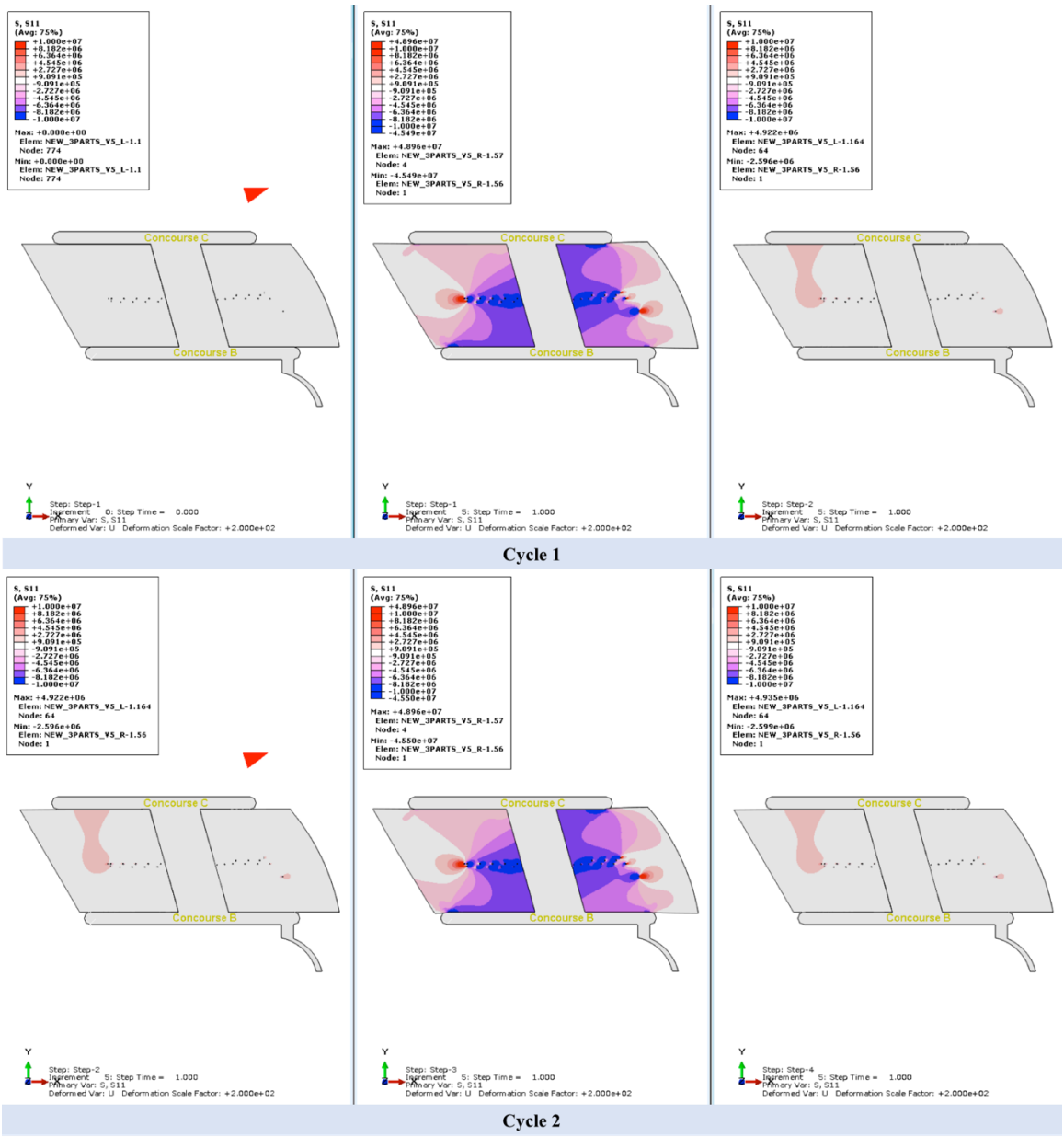

Figure 3.16: Normal stress of slabs in X direction in model with utility vaults, by Pa. (left: -5 ºC center: 15 ºC right: -5 ºC)

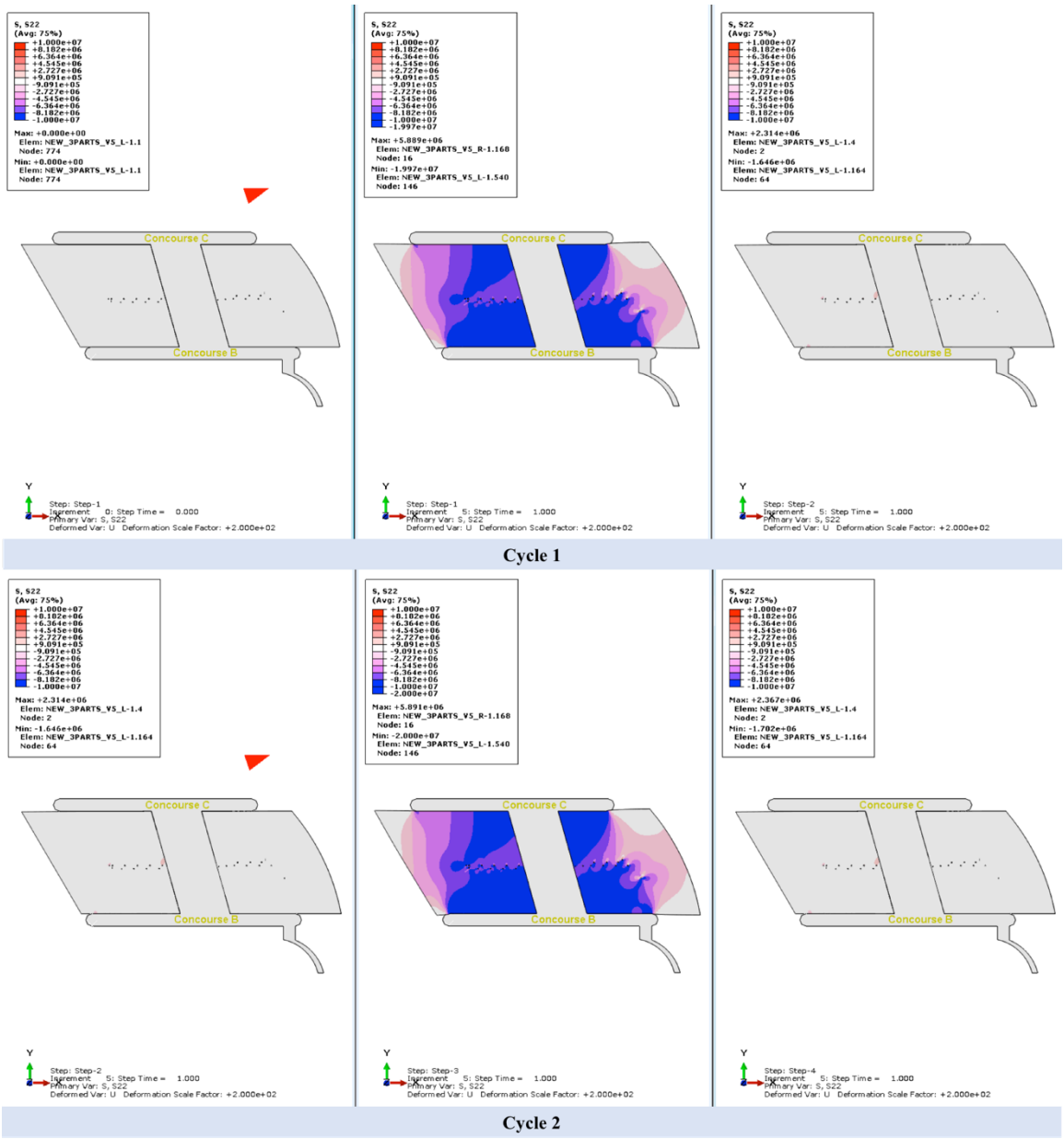

Figure 3.17: Normal stress of slabs in Y direction in model with utility vaults, by Pa. (left: -5 ºC center: 15 ºC right: -5 ºC)

3.4 Consideration of slab partition

For simplification, two single large slabs were assumed in the basic model as discussed towards the beginning of this chapter. To evaluate the influence of this simplification, a model considering slab partition is investigated. The layout of the model with slab partition is shown in Figure 3.18, in which the slab part at the south side was divided into nine pieces and the one at the north side was preserved for comparison purposes. The "hard contact" mode was assumed between the newly divided slabs. Other input parameters of the model were preserved. Only one complete temperature cycle between -5 ºC to 15 ºC was applied in the simulation.

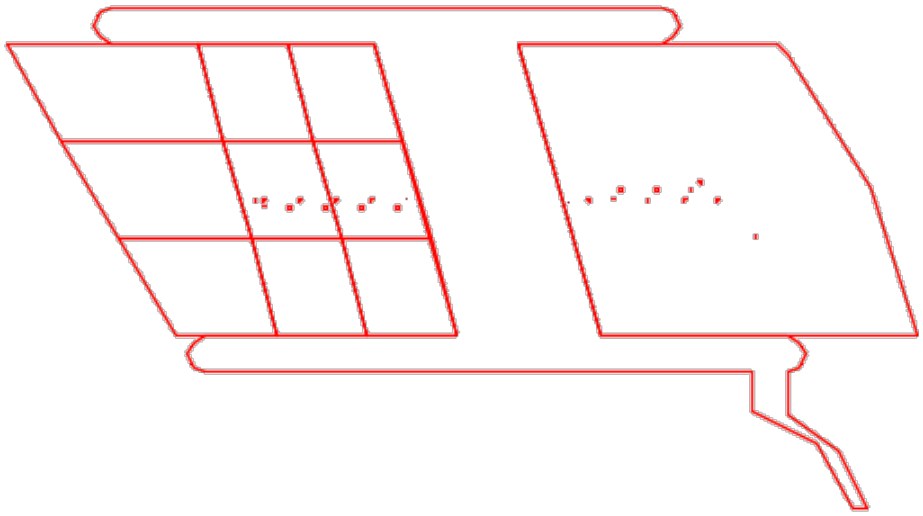

Figure 3.18: Geometry layout of model with slab partition.

The outputs of slab deformation and stress distribution of the model with slab partition are given in Figure 3.19 to 3.22. The displacement result shown in Figure 3.19 is slightly different from that of the single-part model shown in Figure 3.8. According to Figure 3.19, the "fixed points" in the model with slab partition are located only on two of the newly divided slabs, resulting in a relatively free movement of the other slabs. Therefore, the displacement near the free edges from

the model with slab partition is slightly higher. However, the overall displacement responses with and without slab partition are similar. Similarly, the stress distribution of the multi-part model shown in Figure 3.20 to 3.22 has limited changes to those of the single-part model.

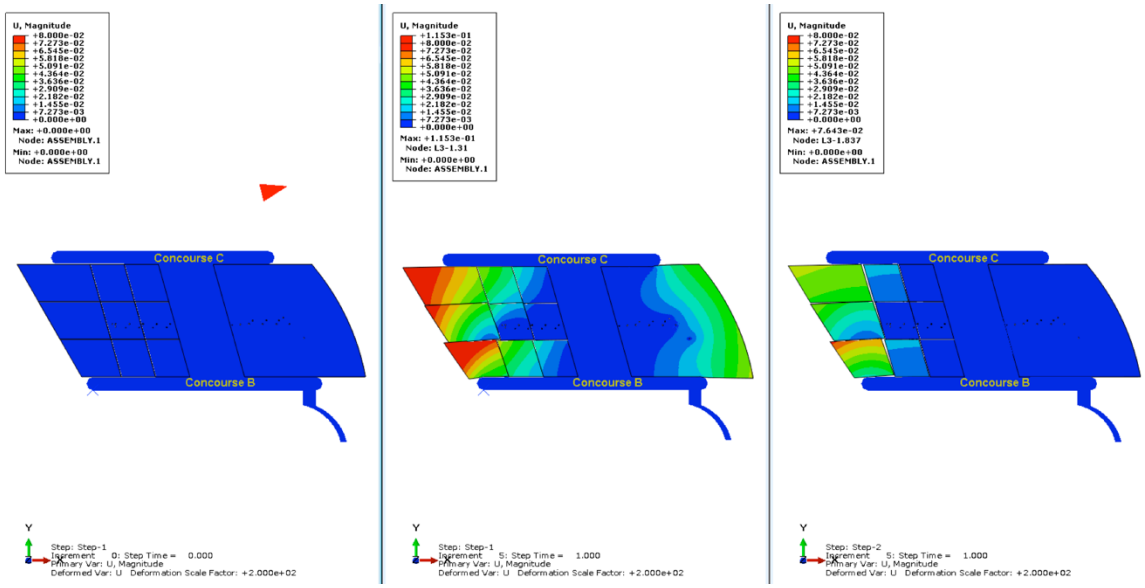

Figure 3.19: Displacement of slabs in the model with slab, by m.
(left: -5 ºC center: 15 ºC right: -5 ºC)

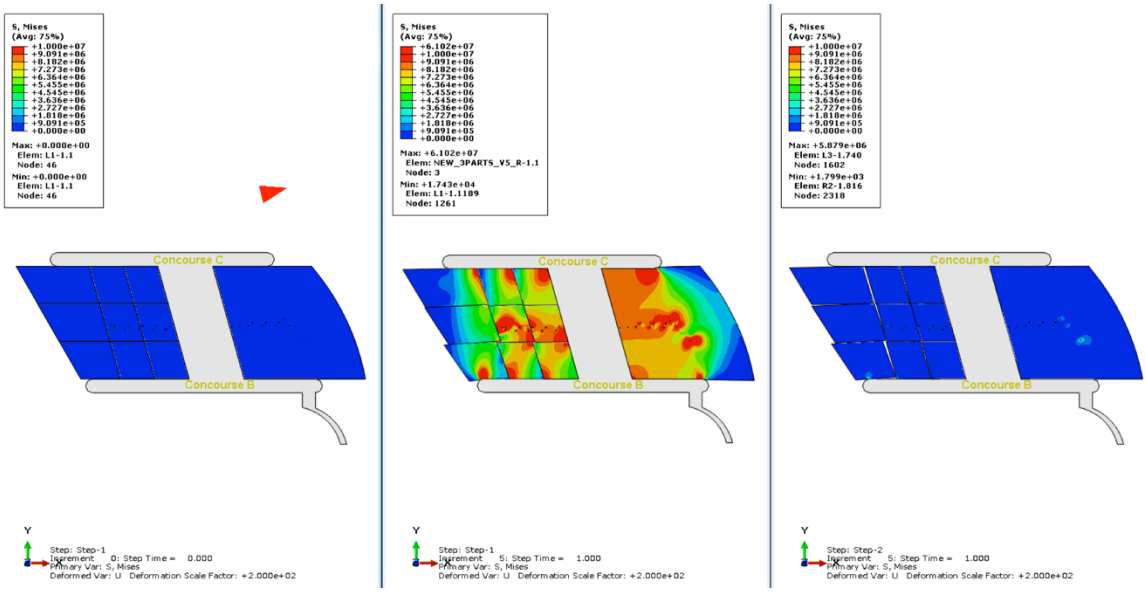

Figure 3.20: Effective stress of slabs in the model with slab partition, by Pa.
(left: -5 ºC center: 15 ºC right: -5 ºC)

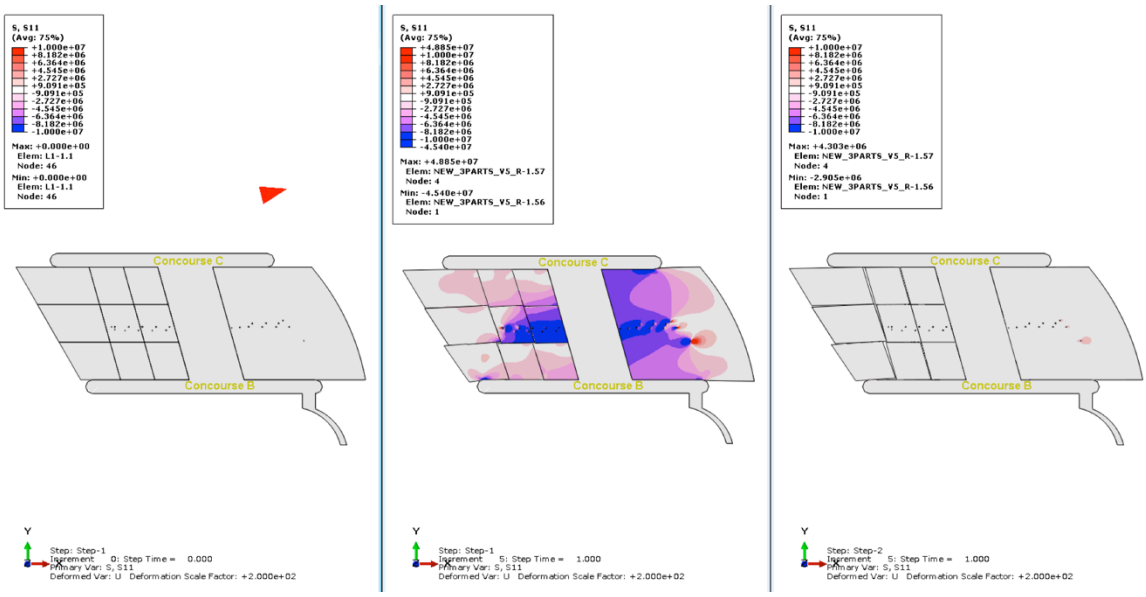

Figure 3.21: Normal stress of slabs in X direction in the model with partition, by Pa. (left: -5 ºC center: 15 ºC right: -5 ºC)

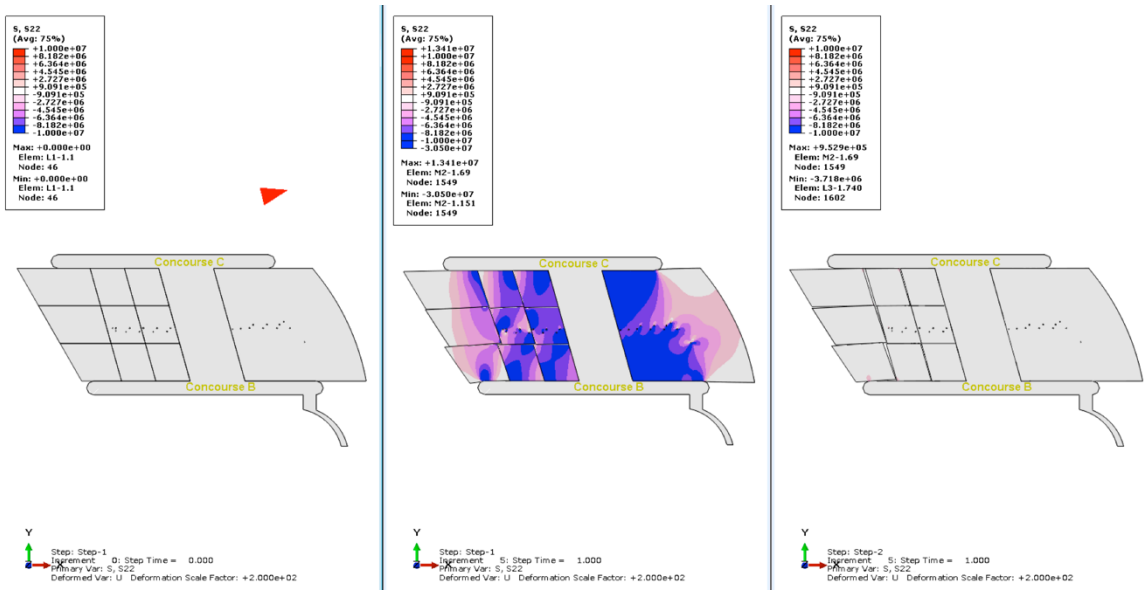

Figure 3.22: Normal stress of slabs in Y direction in the model with partition, by Pa. (left: -5 ºC center: 15 ºC right: -5 ºC)

Overall, no essential difference is found before and after the slab partition, and therefore, it is unnecessary to divide the slab during the modeling process.

3.5 Incorporation of joint at the tunnel boundary

The expansion joints isolating the tunnel and the outer concrete slabs makes a difference on the slab movement. To account for this factor, the model with the utility vaults is further developed to incorporate influence from the expansion joint. The layout of the modified model is shown in Figure 3.23, where a gap is left in between the slabs and the tunnel as the expansion joint. The expansion joint was only introduced to the slab part at the south side. To allow a full separation, the joint width was assumed to be 500 mm. Silicone rubber was selected as the sealant material modelled in the gap with a density of 1100 kg/m^3, a Young's modulus of 0.001 GPa, a Poisson's ratio of 0.47 and a coefficient of thermal expansion of 2.5 E-4/ºC [28]. Other parameters were preserved from the model discussed in Section 3.3. The same temperature cycle between -5 ºC and 15 ºC to -5 ºC was applied.

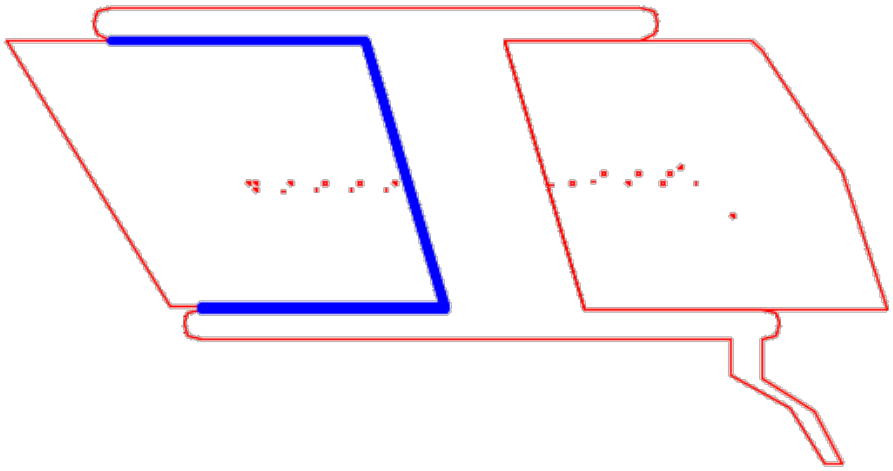

Figure 3.23: Geometry layout of the model with expansion joint.

The outputs of slab deformation and stress distribution of the model with gap opening and the sealant are shown in Figure 3.24 to 3.27. During the temperature rise, due to existence of the

expansion joint, the slab expands freely in both X and Y directions, as indicated by Figure 3.24. As for the effective stress of the model shown in Figure 3.25, the stress is only concentrated near the utility vaults. Comparing to Figure 3.15, the stress concentration near the boundary in Figure 3.25 is successfully released by the expansion joint.

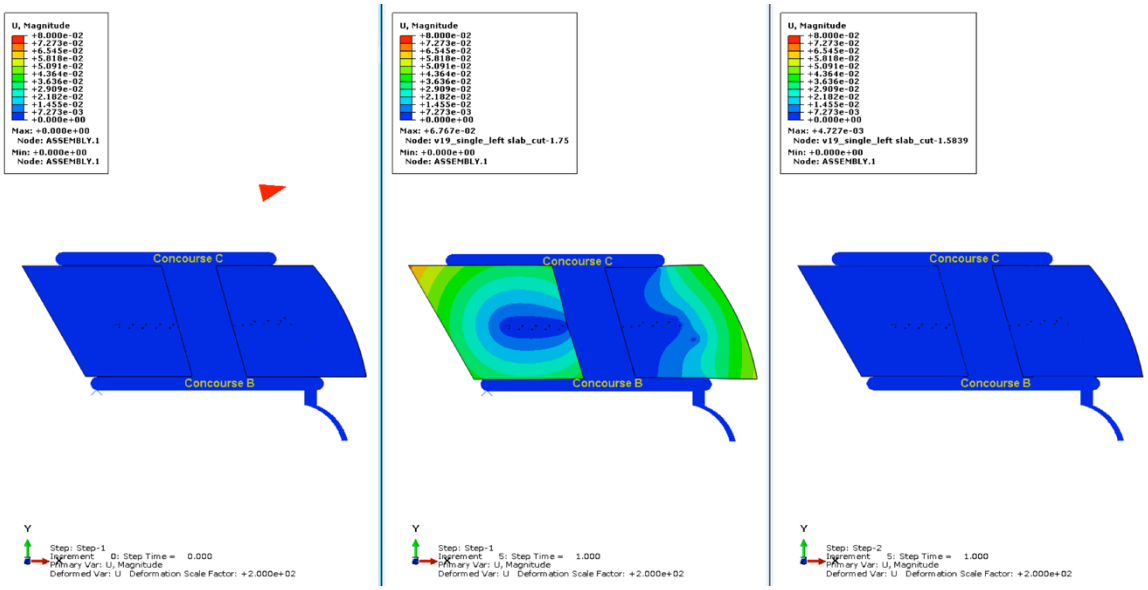

Figure 3.24: Displacement of slabs in the model with expansion joint, by m.
(left: -5 ºC center: 15 ºC right: -5 ºC)

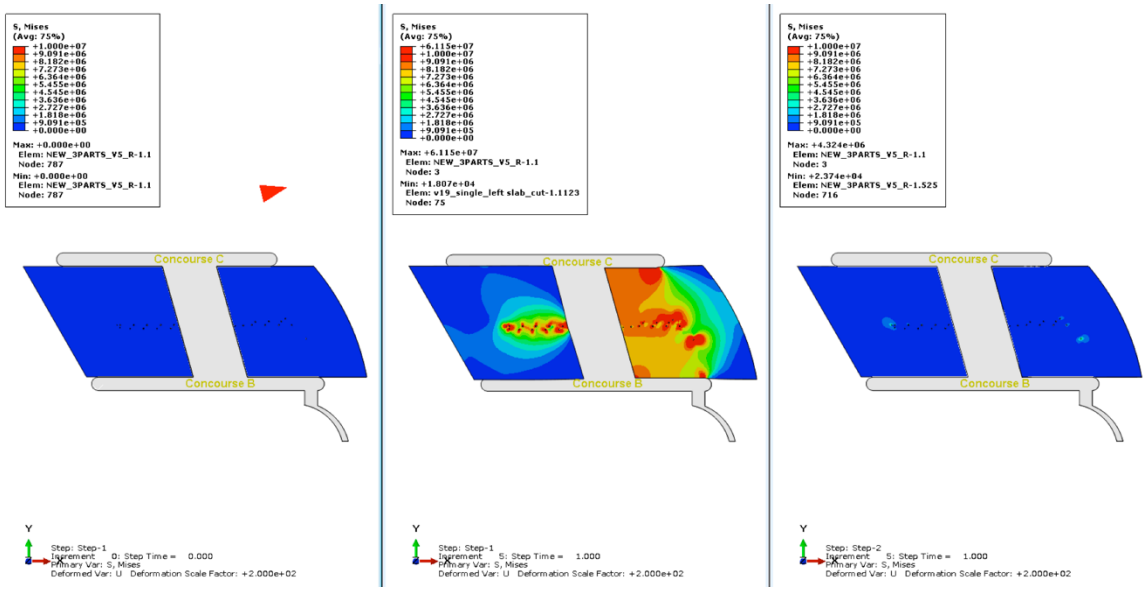

Figure 3.25: Effective stress of slabs in the model with expansion joint, by Pa.
(left: -5 ºC center: 15 ºC right: -5 ºC)

Comparing to the normal stress results of the model without expansion joint shown in Figure 3.16 and 3.17, the normal stress in Y direction shown in Figure 3.27 is greatly released. In comparison, less stress is released in X direction, as only the inner side is confined in the previous model.

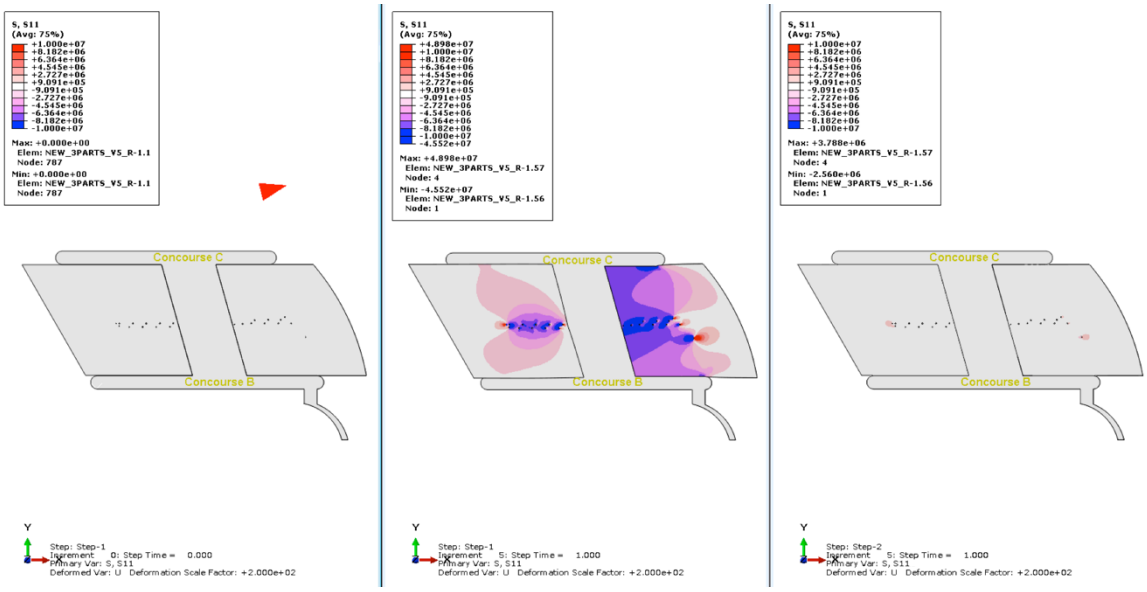

Figure 3.26: Normal stress of slabs in X direction in model with expansion joint, by Pa. (left: -5 ºC center: 15 ºC right: -5 ºC)

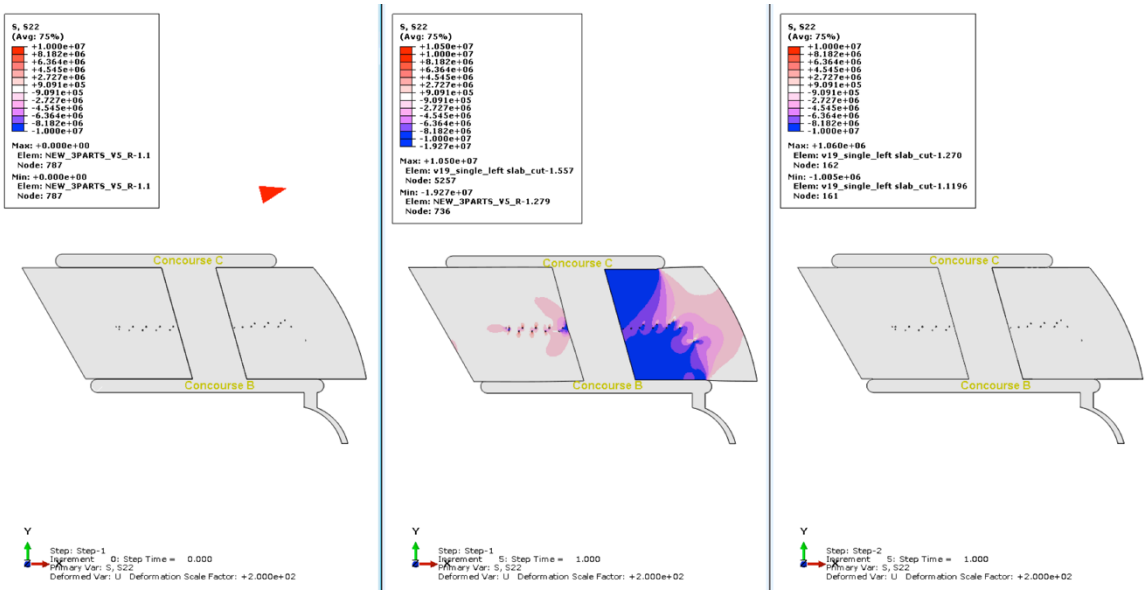

Figure 3.27: Normal stress of slabs in Y direction in model with expansion joint, by Pa. (left: -5 ºC center: 15 ºC right: -5 ºC)

Due to the significant differences induced by the expansion joint, both utility vaults and expansion joints are adopted in the final model.

3.6 Comparison of predicted joint opening to field measurement

To evaluate the accuracy of the FEM simulation, the simulated joint opening was compared to that obtained from the field manual measurement. As the average temperature change between the manual inspection conducted at May 2nd and Aug 9th was +10 ºC, the same temperature change of +10 ºC was used in the FEM analysis. The simulated displacement results in X direction is shown in Figure 3.28. In correspondence to the actual inspection locations, special attention was paid to the six points located along the expansion joints between the slabs and the B-C tunnel, which are highlighted as red dots in the figure. The displacement results of the six points were compared with the field measurement in Table 3.2.

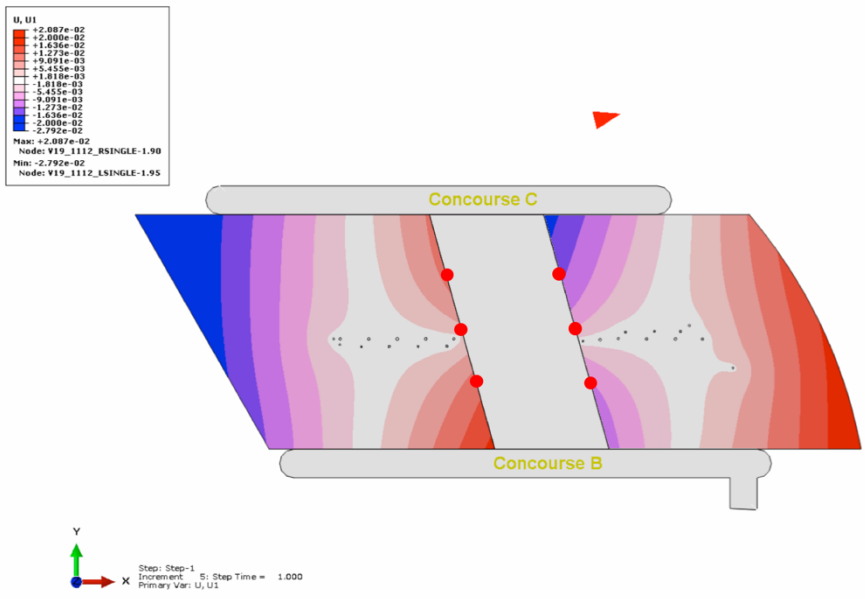

Figure 3.28: Displacement of slabs in X direction under 10 ºC temperature rise.

Table 3.2: Comparison of displacement in field and in model

	South (left)		North (right)	
	Field (mm)	Model (mm)	Field (mm)	Model (mm)
West (up)	4.39	9.51	10.02	13.70
Middle	6.78	4.04	5.60	5.31
East (down)	9.30	10.09	6.73	8.93

Comparing the two groups of displacement results in Table 3.2, the simulated results are reasonably close to the field measurement. In addition, the trend that the openings are smaller in the middle as revealed by the simulation gets confirmed by the field measurement. Therefore, the FEM simulation is proven to be successful, and the modeling result is sufficiently accurate to predict the response of the concrete slabs in a realistic way.

3.7 Stress concentration in tunnel slab

Evidence of edge damage of the concrete slabs is observed near the tunnel, as shown in Figure 3.2. It is suspected that this kind of damage was caused by insufficient stress release between the slabs. In other words, the damage could be related to the width of the expansion joints. To evaluate the influence of the joint width on the stress concentration in the tunnel region, three joint openings were studied, i.e. 0, 20 mm, and 30 mm. During the FEM simulation, one complete temperature cycle between -5 ºC and 15 ºC was applied.

The effective stress distributions in the tunnel region are shown in Figure 3.29. The results of 0, 20-mm, 30-mm expansion joint are given left to right. Without a joint, the maximum stress in the

tunnel is found to be 3.608 MPa, which is sufficiently high to cause the damage to the tunnel structure in a long term. In the case of the 20-mm joint, the maximum stress is greatly reduced to 1.285 MPa, which is only about 1/3 of the previous case. Concurrently, an overall reduction of the stress distribution is seen across most of the tunnel region, as suggested by the color change in the figure. In the case of the 30-mm joint, the maximum stress is further reduced to 0.2502 MPa, which is less than 1/10 of the maximum stress in the worst-case scenario without a joint. Evidently, stress concentration across the tunnel region is almost fully released, suggesting that the 30-mm expansion joint has a great potential to reduce the risk of structure damage in the tunnel. Assuming the tunnel is currently suffering from the worst-case scenario, an additional 30-mm for the expansion joint is recommended for the subsequent repair works to prevent reoccurrence of the tunnel damage in the future.

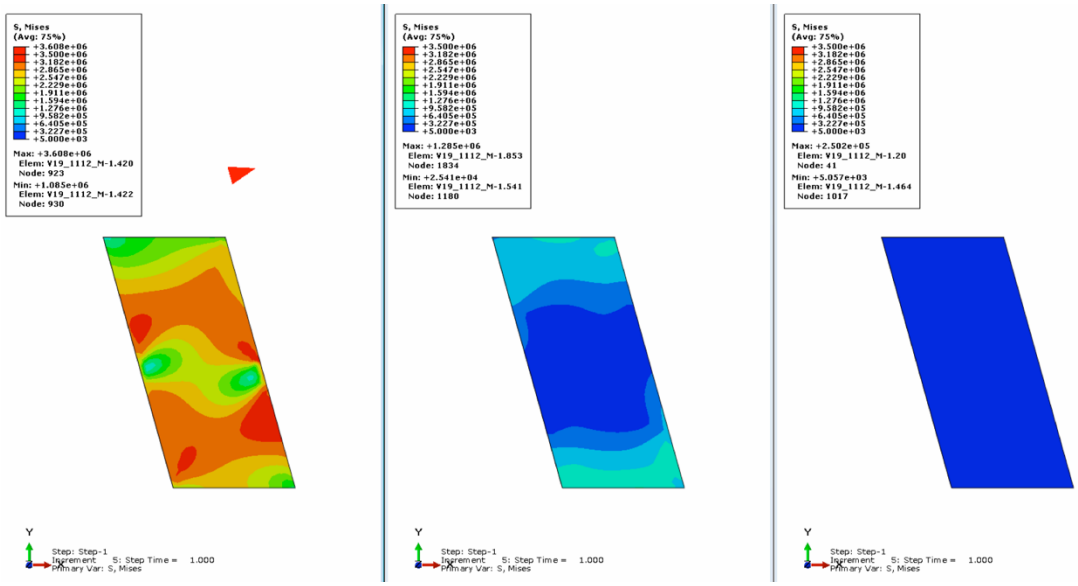

Figure 3.29: Stress concentration in tunnel.
(left: 0 center: 20-mm right 30-mm)

CHAPTER 4. SUMMARY

Two investigations were conducted using FEM simulation, which showed the advantages of using FEM in understanding concrete material behavior on different scales. In the foam concrete study, an approach was proposed that can investigate real foam concrete cellular structure from a micro level. With a micro-CT scan providing the geometry information, the foam concrete microstructure was restored by creating volumetric tetrahedral meshes. A uniaxial compression test was simulated in Abaqus/CAE by assigning a vertical displacement on top of the foam concrete model. As the microstructure deformed, the stress concentration initiated from the cell walls. The simulation result was reasonable from a qualitative perspective. As such, there is a good potential of using this approach for further predicting foam concrete crushing behavior. Future works will focus on improving the simulation accuracy by introducing the material failure model. Ultimately, this modeling approach should provide insights of constructing the material constitutive relationship, which is essential for the material research on foam concrete.

As for the inspection of full-scale airport slab movement, four model configurations of the slabs with varying considerations were evaluated. The modeling effort demonstrated that inclusion of the utility vaults and the expansion joint contributed to reason FEM predictions that were matched with the field measurements with respect to the joint opening results. It was recognized that a sufficient expansion joint width was critical to release the stress buildup in the tunnel region. To prevent reoccurrences of the tunnel damage in the future, this study concludes that an additional 30-mm opening for the expansion joint is recommended for the subsequent repair works.

REFERENCES

[1] M. R. Jones and A. McCarthy, “Preliminary views on the potential of foamed concrete as a structural material,” Mag. Concr. Res., vol. 57, no. 1, pp. 21–31, 2005.

[2] R. Valcore, “Cellular concretes part 2 physical properties,” ACI J. Proc., vol. 50, no. 6, pp. 817–836, 1954.

[3] A. Short and W. Kinniburgh, Lightweight concrete, 3rd ed. London: Applied Science Publishers, 1978.

[4] ACI Committee 229, “Report on Controlled Low-Strength Materials,” Farmington Hills, MI, 2013.

[5] G. Gonzalez and H. K. Moo-Young, “Transportation applications of recycled concrete aggregate,” 2004.

[6] R. Jones, L. Zheng, A. Yerramala, and K. S. Rao, “Use of recycled and secondary aggregates in foamed concretes,” Mag. Concr. Res., 2012.

[7] R. Serpell, J. Henschen, J. Roesler, and D. Lange, “Relative proportioning method for controlled low-strength material,” ACI Mater. J., 2015.

[8] K. Ramamurthy, E. K. Kunhanandan Nambiar, and G. Indu Siva Ranjani, “A classification of studies on properties of foam concrete,” Cem. Concr. Compos., 2009.

[9] S. Mindess, Developments in the Formulation and Reinforcement of Concrete. 2008.

[10] K. S. Al-Jabri, A. W. Hago, A. S. Al-Nuaimi, and A. H. Al-Saidy, “Concrete blocks for thermal insulation in hot climate,” Cem. Concr. Res., vol. 35, no. 8, pp. 1472–1479, 2005.

[11] R. Valcore, “Insulating concretes,” ACI J. Proc., vol. 53, no. 11, pp. 509–532, 1956.

[12] M. S. Al-Homoud, “Performance characteristics and practical applications of common building thermal insulation materials,” Build. Environ., vol. 40, no. 3, pp. 353–366, 2005.

[13] D. Lange, Y. Song, K. Hawkins, and J. Clark, “Recycled concrete used to create novel foamed materials,” Research on Concrete Application for Sustainable Transportation, vol. 4, no. 1, 2017.

[14] M. F. Ashby, “Mechanical Properties of Cellular Solids.,” Metall. Trans. A, Phys. Metall. Mater. Sci., vol. 14 A, no. 9, pp. 1755–1769, 1983.

[15] “Engineered Materials Arresting Systems (EMAS) for aircraft overruns,” 2012.

[16] M. Alexander-Adams, “Fact Sheet- Engineered Material Arresting System (EMAS),” Federal Aviation Administration, 2016. [Online]. Available:

https://www.faa.gov/news/fact_sheets/news_story.cfm?newsId=13754.

[17] L. J. Gibson and M. F. Ashby, Cellular solids: Structure and properties, vol. 123. 1990.

[18] O. Coussy, Mechanics and Physics of Porous Solids. 2010.

[19] M. Scheffler and P. Colombo, Cellular Ceramics: Structure, Manufacturing, Properties and Applications. 2006.

[20] Y. Song and D. A. Lange, "Crushing behavior of foam concrete," in The 9th International Symposium on Cement & Concrete (ISCC), 2017.

[21] J. Schindelin et al., "Fiji: An open-source platform for biological-image analysis," Nature Methods, vol. 9, no. 7. pp. 676–682, 2012.

[22] "Thresholding," ImageJ, 2016. [Online]. Available: https://imagej.net/Thresholding.

[23] S. Tada and S. Nakano, "Microstructural approach to properties of moist cellular concrete," in Proceedings Autoclaved Aerated Concrete, Moisture and Properties, 1983, pp. 71–89.

[24] Q. Fang and D. A. Boas, "Tetrahedral mesh generation from volumetric binary and grayscale images," in Proceedings - 2009 IEEE International Symposium on Biomedical Imaging: From Nano to Macro, ISBI 2009, 2009, pp. 1142–1145.

[25] A. Liu and B. Joe, "Relationship between tetrahedron shape measures," Bit, vol. 34, no. 2, pp. 268–287, 1994.

[26] P. Domono and J. Illston, Construction Materials. London: CRC Press, 2010.

[27] S. Mindess, J. Young, and D. Darwin, Concrete, 2nd ed. Upper Saddle River, NJ: Pearson Education, Inc., 2003.

[28] "Silicone Rubber," AZO Materials. [Online]. Available: https://www.azom.com/properties.aspx?ArticleID=920.

APPENDIX A: PARTIAL CODE FOR USING DIFFERENT MESHING METHODS

```
% cgalpoly method
tic
[no,el]=vol2surf(cleanimg,ix,iy,iz,opt,1,'cgalpoly');
[node,elem,face]=cgals2m(no(:,1:3),el(:,1:3),opt,maxvol);
toc

% cgalsurf method
tic
[no,el,regions,holes]=vol2surf(cleanimg,ix,iy,iz,opt,1,'cgalsurf');
[node,elem,face]=surf2mesh(n1,el,[],[],keepratio,maxvol,[],[],[]);
toc

% cgalmesh method
tic
[node,elem,face]=vol2mesh(cleanimg,ix,iy,iz,opt,maxvol,1,'cgalmesh');
toc
```